Vanishing White Matter Disease Expression of Truncated EIF2B5 Activates Induced Stress Response

Matthew D. Keefe,[1^] Haille E. Soderholm,[1^] Hung-Yu Shih,[1^] Tamara J. Stevenson,[1] Kathryn A. Glaittli,[1] D. Miranda Bowles,[1] Erika Scholl,[1] Samuel Colby[2], Samer Merchant[2], Edward W. Hsu[2], and Joshua L. Bonkowsky[1,3*]

[1]Department of Pediatrics
University of Utah School of Medicine
Salt Lake City, Utah, USA
[2]Department of Bioengineering
University of Utah
Salt Lake City, Utah, USA
[3]Brain and Spine Center
Primary Children's Hospital
Salt Lake City, Utah, USA

^Co- first authors
*Correspondence: joshua.bonkowsky@hsc.utah.edu

Abstract

Vanishing White Matter disease (VWM) is a severe leukodystrophy of the central nervous system caused by mutations in subunits of the eukaryotic initiation factor 2B complex (eIF2B). Current models only partially recapitulate key disease features, and pathophysiology is poorly understood. Through development and validation of zebrafish (*Danio rerio*) models of VWM, we demonstrate that zebrafish *eif2b* mutants phenocopy VWM, including impaired somatic growth, early lethality, impaired myelination, loss of oligodendrocyte precursor cells, increased apoptosis in the CNS, and impaired motor swimming behavior. Expression of human *EIF2B2* in the zebrafish *eif2b2* mutant rescues lethality and CNS apoptosis, demonstrating conservation of function between zebrafish and human. In the mutants, intron 12 retention leads to expression of a truncated *eif2b5* transcript. Expression of the truncated *eif2b5* in wild-type larva impairs motor behavior and activates the ISR, suggesting that a feed-forward mechanism in VWM is a significant component of disease pathophysiology.

Keywords: Vanishing white matter disease (VWM), EIF2B, leukodystrophy, induced stress response, zebrafish, MRI, myelin.

Abbreviations: Vanishing White Matter Disease (VWM); Magnetic Resonance Imaging (MRI); Induced Stress Response (ISR); Polymerase Chain Reaction (PCR); eukaryotic initiation factor 2B (eIF2B); Central Nervous System (CNS)

Introduction

Vanishing White Matter (VWM) disease is a genetic leukodystrophy leading to severe neurological disease and early death (Fogli et al., 2004; van der Knaap et al., 2006; Labauge et al., 2009; Carra-Dalliere et al., 2011; Hamilton et al., 2018). VWM disease is caused by bi-allelic recessive variants in any of the five genes encoding subunits (1-5) of the eukaryotic translation initiation factor 2B (eIF2B) complex. Symptoms of VWM include ataxia, spasticity, seizures, cognitive impairment, and motor problems. While there are no sex differences seen in VWM patients, females can experience ovarian failure. In patients, autopsies have revealed affected oligodendrocytes and astrocytes, myelin loss, and cystic cavitations of white matter (van der Knaap et al., 1997; van der Knaap et al., 1998; Pronk et al., 2006). Genotype-phenotype correlations of mutation severity have been shown (Hamilton et al., 2018), and severe multi-organ involvement is characteristic of fetal and neonatal forms (van der Knaap et al., 2003; Song et al., 2017). Disease onset <4 years of age is followed by a rapid deterioration of symptoms, while disease onset >4 years of age shows greater variability in disease course (Hamilton et al., 2018). There is no treatment for VWM disease, and current mouse models only partially recapitulate disease pathophysiology (Geva et al., 2010; Dooves et al., 2016).

The eIF2B complex is a heteropentameric guanine nucleotide exchange factor (GEF) for eukaryotic initiation factor 2 (eIF2), which governs the rate of global protein synthesis and cap-dependent translation initiation. The eIF2B complex also functions to displace eIF5 from inactive GDP-bound eIF2 to allow its recruitment to the ribosome (Jennings and Pavitt, 2014). Importantly, the eIF2B complex plays a central role in the cellular integrated stress response (ISR). Stress-dependent kinase activation leads to phosphorylation of eIF2, which binds eIF2B more tightly and reduces overall protein synthesis (Krishnamoorthy et al., 2001; Pakos-

Zebrucka et al., 2016). In human cell lines, it has been shown that translation is suppressed to a greater degree after stress in VWM patients (Moon and Parker, 2018). This suppression of translation lasts for a longer period of time in VWM cells, and the protein responsible for de-phosphorylating eIF2 and allowing translation recovery, GADD34, was found in lower quantities.

Mouse lines with knock-in/knock-out mutations in *Eif2b5*^{R132H}, a common allele of VWM patients, have impaired motor function, growth deficits, delayed development of white matter, and abnormal abundance of oligodendrocytes and astrocytes (Geva et al., 2010; Atzmon et al., 2018). This developmental role for eIF2B was further confirmed in a mouse model with developmental misexpression of pancreatic endoplasmic reticulum kinase (PERK) in oligodendrocytes. PERK is one of the stress-responsive kinases that activate the ISR via phosphorylation of eIF2. PERK misexpression caused hypomyelination, oligodendrocyte damage, and myelin loss (Lin et al., 2014). However, this result was only seen in young mice, and could not be induced in mature animals.

ISR activation has been identified in VWM patient brain autopsy samples (van Kollenburg et al., 2006) and in mouse VWM models (Wong et al., 2019; Abbink et al., 2019). A small molecule inhibitor of the ISR, ISRIB, has been shown to bind to and activate the decameric, functional eIF2B complex (Sidrauski et al., 2013; Sidrauski et al., 2015; Wong et al., 2018).

There are key aspects that remain unclear about eIF2B function and its involvement in VWM pathophysiology. eIF2B is expressed globally but VWM primarily affect the CNS, including differential effects in the CNS. For example, oligodendrocyte numbers are decreased in affected white matter, but they are increased in other areas (van Haren et al., 2004; Bugiani et al.,

2010). GEF activity of the eIF2B complex does not appear to correlate with VWM disease severity (Liu et al., 2011), suggesting that the overall protein translation is not the key component of VWM pathophysiology. Another unusual and poorly understood aspect of VWM is that rapid clinical deterioration and white matter loss can be provoked by a stressor, such as minor head trauma or mild illness (van der Knaap et al., 2006). This is consistent with models in which chronic ISR activation cause cellular apoptosis (Bond et al., 2020), but the mechanism by which VWM mutation affects ISR response is unclear. Further, there is some evidence that a de-regulated ISR is not alone sufficient to cause VWM pathology (Wisse et al., 2018), and in fact blocking the ISR worsens VWM pathology (Sekine et al., 2016). Thus, current models and approaches have left key questions unanswered.

We report the development and characterization of a small vertebrate (zebrafish – *Danio rerio*) model of VWM. We have generated and characterized mutant alleles in zebrafish *eif2b* subunits 1, 2, and 4, and an allelic series in subunit 5. We demonstrate that the *eif2b* mutants exhibit a range of phenotypic severity, including changes in growth, lethality, behavior, myelination, apoptosis and proliferation in the CNS. We also show conservation of function of *eif2b2* between zebrafish and humans, validating the zebrafish model for understanding human VWM. We find that the *eif2b* mutants at baseline have activated induced stress response (ISR). The zebrafish *eif2b* mutants have impaired swimming motor behavior, a phenotype that could be used in a phenotype-based screen. Finally, we found that in the zebrafish *eif2b* mutants, a truncated *eif2b5* transcript is generated. The truncated *eif2b5* is capable of activating the ISR, and can impair motor behavior, suggesting that a feedback loop with truncated *eif2b5* may play an important role in disease pathology. Our work reveals a similar role for the *eif2b* complex in

zebrafish and in humans, identifies a novel mechanism of VWM pathophysiology, and provides a useful model of VWM for future therapeutics screening.

Results

Phylogenetic analysis of EIF2B sequence homology and expression in zebrafish development

We characterized the sequence and developmental expression of the five Eif2b subunit orthologs in zebrafish, *eif2b1-5* (*eif2b1*, ENSDARG00000091402; *eif2b2* ENSDARG00000041397; *eif2b3*, ENSDARG00000018106; *eif2b4*, ENSDARG00000014004; *eif2b5*, ENSDARG00000074995). Each human *EIF2B* subunit gene has a single zebrafish ortholog with a conserved amino acid sequence (**Figure 1A**). The Eif2b zebrafish and human protein structures also show conserved structural domains (**Figure 1B)**. We evaluated *eif2b* genes expression during early development. Expression analysis of zebrafish *eif2b* genes at 24 hpf (hours post-fertilization) showed expression chiefly in the brain and eye (**Figure 1C-G**). By 72 hpf expression was clearly noted throughout the animal, with higher levels in the brain **(Figure 1H-L)**. Quantitative RT-PCR analysis revealed sub-unit specific expression changes in the first seven days of life **(Figure 1M-Q)**.

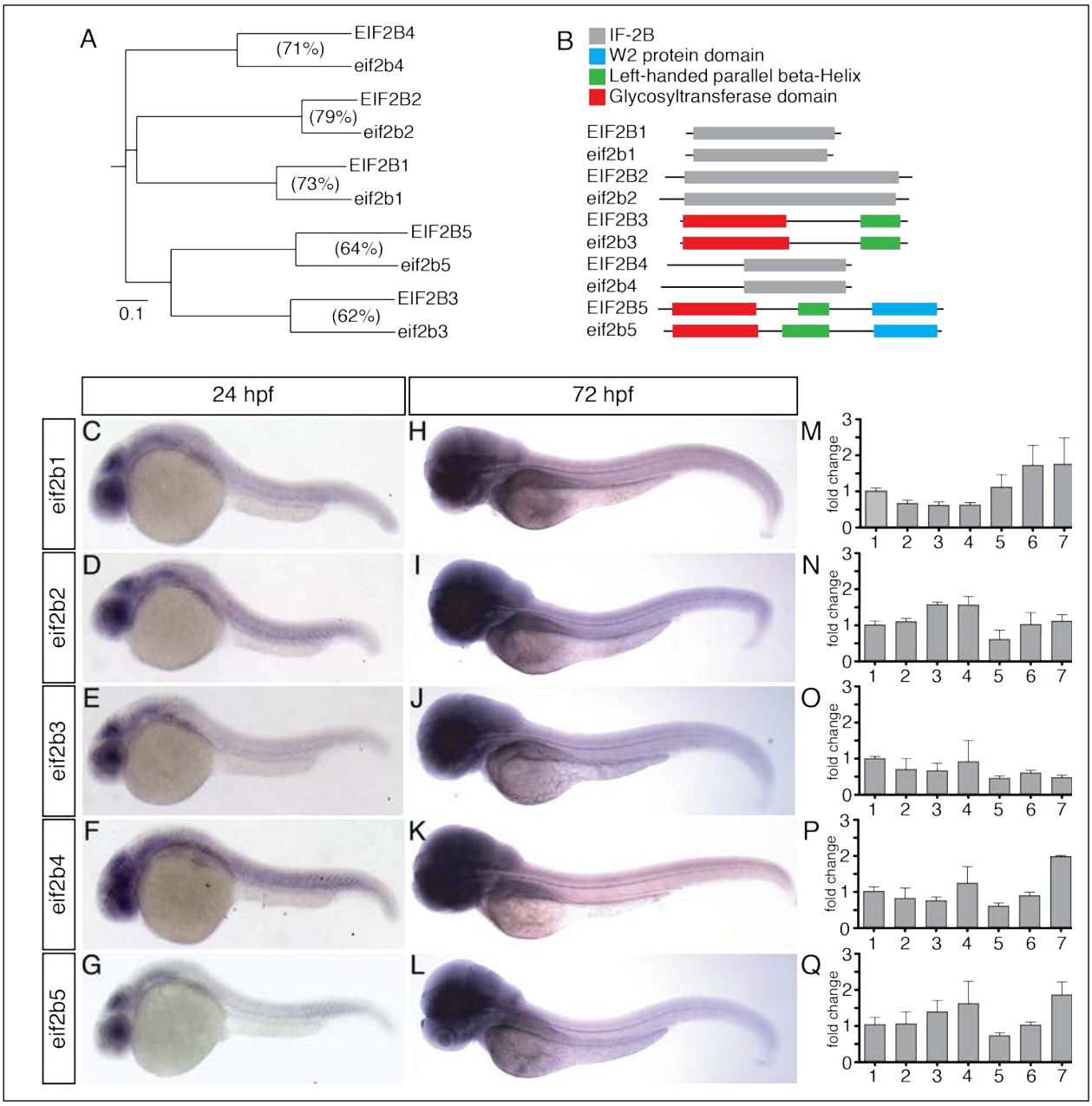

142 **Figure 1.**

143 **Figure 1**. Phylogenetic and expression analysis of Eif2b orthologs in zebrafish during
144 development. (A) A horizontal cladogram of *eif2b1-5* gene sequences shows that zebrafish have
145 a single ortholog of each human *EIF2B* gene, and a relative conservation of amino acid sequence
146 between orthologs. Scale bar equals an evolutionary distance of 0.1 amino acid changes per
147 position in the sequence (Phylodendron). (B) Comparison of zebrafish and human EIF2B protein
148 sequences shows conserved domain architectures. (C-L) Whole mount *in situ* expression analysis
149 in zebrafish embryos and larvae, brightfield microscopy, rostral left, dorsal top. (C-E) *eif2b*
150 subunit genes at 24 hpf shows predominantly brain and eye expression, with lower levels of
151 expression throughout the embryo. (H-L) *eif2b* subunit genes at 72 hpf shows higher expression
152 throughout the animal and in the brain compared to 24 hpf. (M-Q) qRT-PCR expression of *eif2b*

subunit genes from 24 hpf through 7 dpf, normalized to 24 hpf expression demonstrates variable expression changes across development.
Figure 1- Source Data 1: Quantification of qRT-PCR results of eif2b subunits.

Zebrafish *eif2b* subunit mutant alleles generation and molecular characterization

We obtained zebrafish mutant alleles for three *eif2b* subunit genes from the Sanger Institute Zebrafish Mutation Project (*eif2b1*, ENSDARG00000091402; *eif2b2* ENSDARG00000041397; *eif2b4*, ENSDARG00000014004) (**Figure 2A-C)** (15). *eif2b1* (sa12357) harbors a T/A transversion resulting in an early stop in exon 8 (**Figure 2A**); *eif2b2* (sa17223) has a G/A transition in exon 5, mutating an essential splice site (**Figure 2B**); and *eif2b4* (sa17367) has a G/A transition in exon 12 mutating an essential splice site **(Figure 2C)**. To mutagenize subunit *eif2b5*, we used the Clustered Regularly Interspaced Short Palindromic Repeats (CRISPR)/Cas9 system and created six different alleles by targeting exon 1 **(Figure 2D)**. This created three alleles (*zc101*, *zc103*, and *zc104*) with in-frame deletions leading to loss of amino acids; two alleles with a combination of amino acid loss and missense mutations (*zc105* and *zc106*); and one allele (*zc102*) with a nonsense mutation that caused a frame shift in exon 1 leading to a premature stop codon in exon 2. Following CRISPR mutagenesis, individual G0 fish were outcrossed to wild-type animals and offspring were screened by high-resolution melt analysis (HRMA) PCR (Xing et al., 2014). In addition to HRMA PCR genotyping, we confirmed genotypes by Sanger sequencing both in the G0 and subsequent generations. cDNA sequencing of *eif2b2*^{sa17223}, *eif2b5*^{zc102} and *eif2b5*^{zc103} confirmed that the

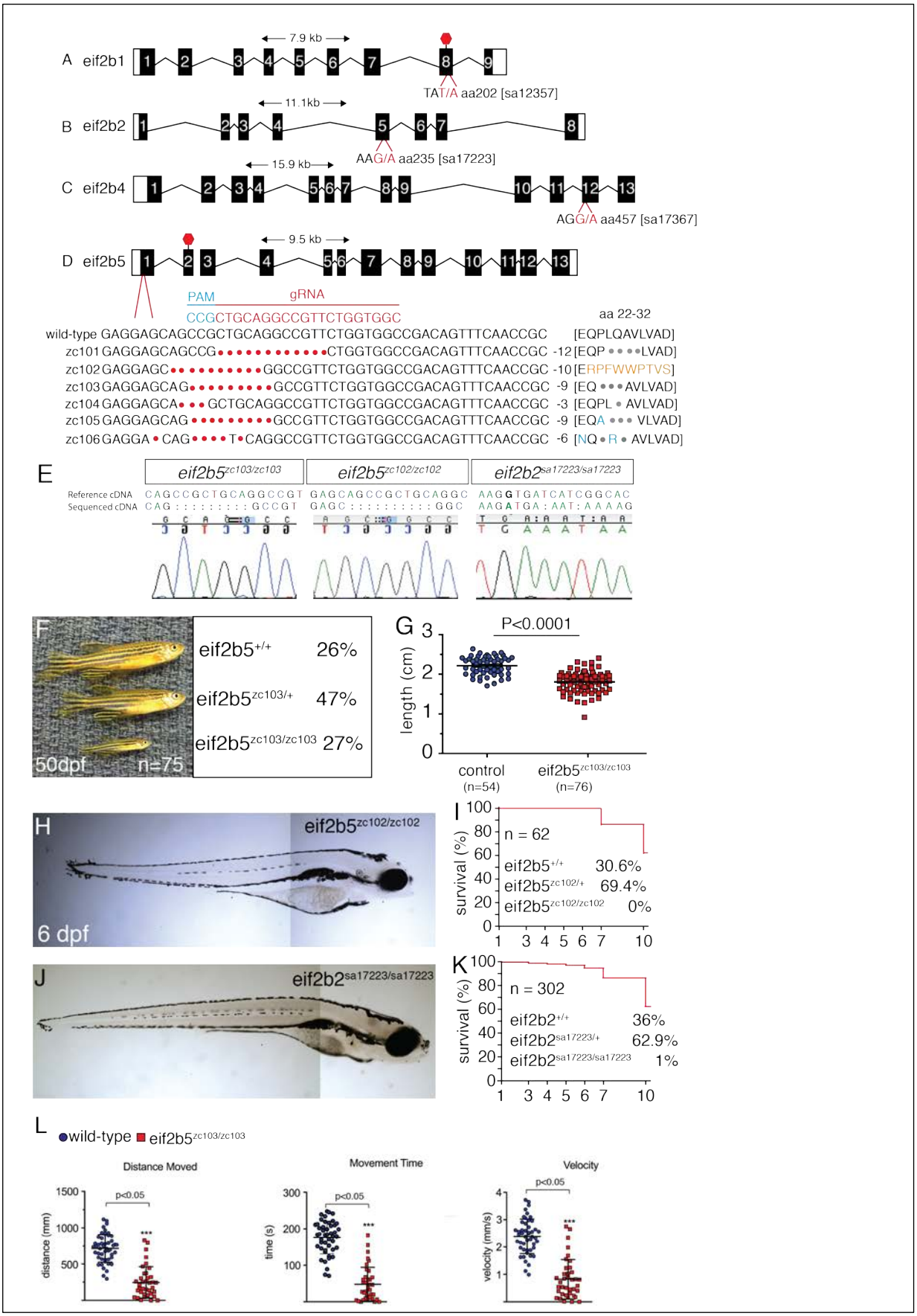

2E). We tried western blotting with several commercial antibodies against Eif2b2 and Eif2b5 (Eif2B2 Abcam 133848; Eif2B5 Abcam ab91563, GeneTex 30808, Santa Cruz 514056, ProSci 56-847, Bethyl A302-557A) but none gave a specific band.

Figure 2. Zebrafish *eif2b* allele generation and characterization. A-D Depiction of zebrafish *eif2b* subunits exon structure and the location and nucleotide change for each mutant. (A) *eif2b1* harbors a T/A transversion resulting in an early stop in exon 8. (B) *eif2b2* has a G/A transition in exon 5, mutating an essential splice site. (C) *eif2b4* has a G/A transition in exon 12 mutating an essential splice site. (D) *eif2b5* exon 1 was targeted for mutagenesis using a gRNA (red). Six distinct alleles were recovered (described in text). (E) Chromatograms of cDNA confirm presence of predicted mutations for $eif2b5^{zc103/zc103}$, $eif2b5^{zc102/zc102}$, and $eif2b2^{sa17223/sa17223}$. (F) $eif2b5^{zc103/zc103}$ mutants survive until adulthood in Mendelian ratios, but show grow defects compared to their heterozygous and wild-type siblings. (G) Adult $eif2b5^{zc103/zc103}$ lengths are significantly shorter compared to their wild-type and heterozygous siblings. (H) Bright-field (BF) image of 6 dpf $eif2b5^{zc102/zc102}$ larva shows a lack of swim bladder and a small head. (I) Kaplan-Meyer survival curves from an $eif2b5^{zc102/+}$ heterozygous incross shows that all homozygotes were dead by 10 dpf (total n = 62). (J) Similar to the $eif2b5^{zc102/zc102}$, a BF image of 6 dpf $eif2b2^{sa17223/sa17223}$ shows a lack of swim bladder and a small head. (K) Kaplan-Meyer survival curves from an $eif2b2^{sa17223/+}$ heterozygous incross shows 1% (n=3) homozygote survival at 10 dpf (total n = 302); however no homozygotes live past two weeks of age. (L) Motor swimming analysis shows impaired swimming behavior in mutants. Distance moved, time spent moving, and velocity, for wild-type controls, and $eif2b5^{zc103/zc103}$ mutants, at 5 dpf.
Figure 2- Source Data 1: Quantification of lengths.
Figure 2- Source Data 2: Quantification of behavior results.

Most of the alleles in the different subunits were homozygous viable, and survived to adulthood and were fertile. The $eif2b5^{zc103/zc103}$ mutants showed a decrease in size compared to their wild type and heterozygous siblings (2.2 cm vs 1.8 cm, 0.3 and 0.2 S.D., and $p<0.0001$) **(Figure 2F-G)**. Mutants of a more severe allele, $eif2b5^{zc102/zc102}$, harboring an early stop codon, exhibited growth deficits such as never developing a swim bladder, and were smaller in size compared to their wild type and heterozygous siblings **(Figure 2H)**. This phenotype was also present in the $eif2b2^{sa17223/sa17223}$ allele **(Figure 2J)**. Two alleles did not survive past two weeks of age: $eif2b5^{zc102/zc102}$ and $eif2b2^{sa17223/sa17223}$ (at 10dpf, $eif2b5^{+/+}$ WT n=12; $eif2b5^{zc102/+}$ heterozygous n=26; $eif2b5^{zc102/zc102}$ n=0. $eif2b2^{+/+}$ WT n=68; $eif2b2^{sa17223/+}$

heterozygous n=118; *eif2b2*$^{sa17223/sa17223}$ n=2) **(Figure 2I,K)**. Finally, since affected VWM patients often have progressive motor impairment, we analyzed the functional effects of *eif2b5* mutants on motor behavior. The *eif2b5* zc103 homozygous mutants had reduced distance moved, movement time, and velocity when assayed at 5 dpf (**Figure 2L**).

eif2b mutants had abnormal CNS development

Because we observed that the *eif2b* mutants had early lethality and abnormal growth, we evaluated different CNS markers in early development. For most experiments we compared three *eif2b* alleles: two alleles in two different subunits with early lethality, *eif2b5*^{zc102} and *eif2b2*^{sa17223}; and a homozygous viable allele, *eif2b5*^{zc103}. At 5 dpf, all three of these mutants showed an increase in cell death, quantified using terminal deoxynucleotidyl transferase dUTP nick end labeling (TUNEL) (*eif2b5*^{zc103}: mean=129.1, S.D.=79.5, *eif2b5*$^{+/+}$: mean=12.2, S.D.=9.8, p=0.001; *eif2b5*^{zc102}*: mean=163.7, S.D.=78.2 eif2b5*$^{+/+}$*: mean=18.7, S.D.=10.6 p=2.03 x10*$^{-5}$ *;* *eif2b2*^{sa17223}: mean=202.8, S.D.=60.8: *eif2B2*$^{+/+}$: mean=37.4, S.D.=25.2, p=0.0005) **(Figure 3A-E)**. We also compared counts of cells expressing phospho-histone H3 (pH3), an indicator of cell proliferation. *eif2b5*^{zc103} and *eif2b5*^{zc102} mutants showed no change in pH3 cell counts at 5 dpf compared to controls, but showed a noticeable change in proliferation pattern, specifically the lack of proliferation in the outer perimeter of the eyes (arrow) and the cerebellum (arrowhead), but apparent increased proliferation in the ventricular region (asterisk) (*eif2b5*^{zc103}: mean=247.2, S.D.=44.5, *eif2b5*$^{+/+}$: mean=273.1, S.D.=43.8, p=0.206; *eif2b5*^{zc102}: mean=243.3, S.D.=40.0, *eif2b5*$^{+/+}$: mean=288.3, S.D.=32.0, p=0.0238) **(Figure 3F-H, J).** *eif2b2*^{sa17223} mutants showed a decrease in pH3 cell counts at 5 dpf compared to controls as well as a change in proliferation pattern (*eif2b2*^{sa17223}: mean=185.3,

S.D.=37.8: *eif2b2*$^{+/+}$: mean=271.6, S.D.=46.7, p=0.0004) **(Figure 3I, J).** In the spinal cord, we measured counts of oligodendrocyte precursor cells (OPCs), which give rise to myelin-producing oligodendroglia. We used the Tg(*olig2:dsRed*) line crossed into the *eif2b5*$^{zc103/zc103}$, *eif2b5*$^{zc102/zc102}$ or *eif2b2*$^{sa17223/sa172233}$ background (Kucenas et al., 2008). We observed no change in the number of OPC between two somites directly above the end of the yolk (*eif2b5*^{zc103}: mean=26.6, S.D.=7.55, *eif2b5*$^{+/+}$: mean=30.71, S.D.=,5.88 p=0.278; *eif2b5*^{zc102}: mean=30.6, S.D.=11.0, *eif2b5*$^{+/+}$: mean=36.6, S.D.=9.63, p=0.514; *eif2b2*^{sa17223}: mean=35.8, S.D.=5.36, *eif2b2*$^{+/+}$: mean=39.2, S.D.=4.66, p=0.163) **(Figure 3K-O)**. Lastly, we looked at apoptotic oligodendrocyte precursor cells in the brain by crossing the Tg(*olig2:dsRed*) line into the *eif2b5*$^{zc103/zc103}$, *eif2b5*$^{zc102/zc102}$ or *eif2b2*$^{sa17223/sa172233}$ background and staining with TUNEL. The *eif2b5*$^{zc102/zc102}$ showed a large increase in the number of TUNEL+ OPC cells specifically in the hindbrain (*eif2b5*^{zc102}: mean=17.5, S.D.=3.02, *eif2b5*$^{+/+}$: mean=1, S.D.=1, p=0.00004). The *eif2b5*$^{zc103/zc103}$ and the *eif2b2*$^{sa17223/sa172233}$ alleles also showed a significant increase in the number of TUNEL+ OPC cells in the hindbrain, but less drastic of a change compared to the *eif2b5*$^{zc102/zc102}$ allele (*eif2b5*^{zc103}: mean=3, S.D.=2.26, *eif2b5*$^{+/+}$: mean=0.7, S.D.= 1.06, p=0.0144; *eif2b2*^{sa17223}: mean=3.5, S.D.=1.05, *eif2b2*$^{+/+}$: mean=0.333, S.D.=0.577, p=0.002) **(Figure 3P-T)**.

250

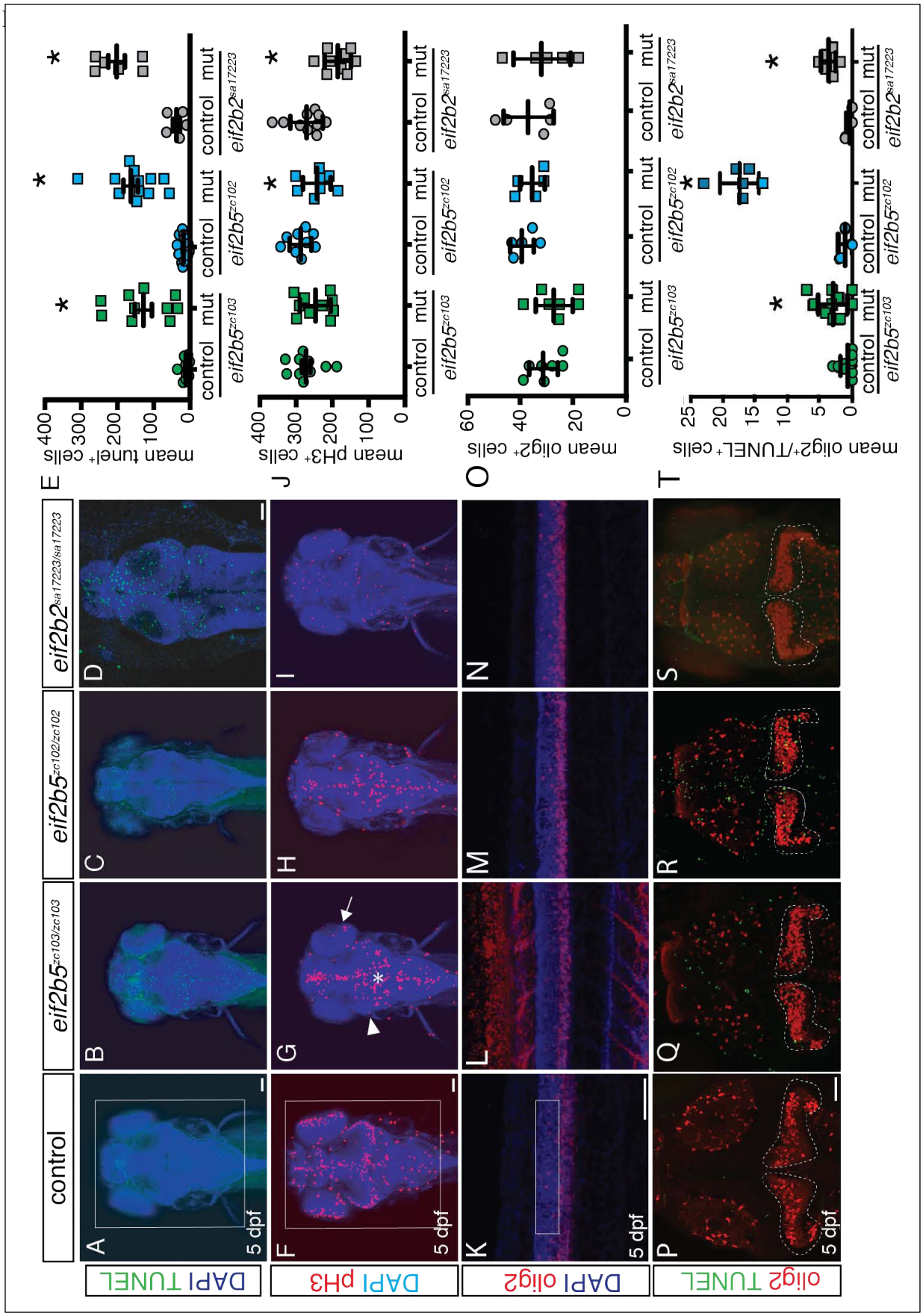

Figure 3. *eif2b* mutants demonstrate abnormal CNS development. Confocal images, z-stack maximal projections. A-I, dorsal views of the brain, rostral to the top, scale bar 50μm; K-N, lateral views of spinal cord, dorsal to the top, scale bar 50um. P-S, dorsal views of brain, rostral to top, scale bar 50μm. * $p < 0.05$. (A-D) TUNEL and DAPI staining shows increased apoptosis in homozygous mutant alleles compared to controls (wild-type and heterozygous siblings) in ei*f2b5*$^{zc103/zc103}$ *eif2b5*$^{zc102/zc102}$ and *eif2b2*$^{sa17223/sa17223}$ mutants. (E) Quantification of mean TUNEL+ cell counts in ei*f2b5*$^{zc103/zc103}$ *eif2b5*$^{zc102/zc102}$ and *eif2b2*$^{sa17223/sa17223}$ mutants compared to sibling controls. (F-I) Phospho-histone 3 and DAPI staining shows decreased cell proliferation in 5 dpf *eif2b2*$^{sa17223/sa17223}$ mutants compared to controls, while ei*f2b5*$^{zc103/zc103}$ *eif2b5*$^{zc102/zc102}$ mutants show a change in proliferation pattern, specifically in the optic tectum. (J) Quantification of mean number pH3+ cells counts in ei*f2b5*$^{zc103/zc103}$ *eif2b5*$^{zc102/zc102}$ and *eif2b2*$^{sa17223/sa17223}$ mutants compared to sibling controls. (K-N) Olig2dsRed and DAPI staining shows no change in oligodendrocyte proliferating cell counts in 5 dpf ei*f2b5*$^{zc103/zc103}$ *eif2b5*$^{zc102/zc102}$ and *eif2b2*$^{sa17223/sa17223}$ mutants compared to controls. (O) Quantification of mean number OPC+ cell counts in ei*f2b5*$^{zc103/zc103}$ *eif2b5*$^{zc102/zc102}$ and *eif2b2*$^{sa17223/sa17223}$ mutants compared to sibling controls.
Figure 3- Source Data 1-4: Quantification of TUNEL, pH3, olig2, and olig2/TUNEL results.

Zebrafish adult *eif2b5*$^{zc103/zc103}$ mutants show myelin defects

VWM patients have a loss of white matter and abnormal white matter signal quality on MRI (Leegwater et al., 2003; van der Knaap et al., 2006). We used transmission electron microscopy (TEM) to measure myelin content in the adult *eif2b5*$^{zc103/zc103}$ mutants compared to age-matched controls. The adult mutants showed a significant decrease in the thickness of the myelin sheath as measured by the G-ratio, the perimeter of the axon to the perimeter of the myelin sheath (*eif2b5*^{zc103}: mean=0.690, S.D.=0.076, *eif2b5*$^{+/+}$: mean=0.593, S.D.= 0.085, p=2.18E-22) **(Figure 4A-E)** . We also performed Black Gold II staining to compare myelination patterns in the CNS. The adult mutants showed a disorganized pattern of myelinated axons in the optic tectum compared to age matched wild type adult controls **(Figure 4F, G)**.

We performed magnetic resonance imaging (MRI) of adult *eif2b5* mutants, and found a decrease in overall brain size in the adult *eif2b5*$^{zc103/zc103}$ mutants compared to adult wild type controls using the skull as a normalization factor to account for the decrease in overall size of

283 the mutants **(Figure 4H-J; Source- Supplemental Figure 1)**. These images showed a decrease
284 in overall brain volume of the *eif2b5*$^{zc103/zc103}$ mutants as measured by length, width and height
285 of the brains compared to age matched controls (*eif2b5*$^{zc103/zc103}$ normalized length:
286 mean=0.933; S.D.=0.041; *eif2b5*$^{+/+}$ normalized length: mean=1.11, S.D.=0.091, p=0.001;
287 *eif2b5*$^{zc103/zc103}$ normalized width: mean=0.836; S.D.=0.034; *eif2b5*$^{+/+}$ normalized width:
288 mean=0.958, S.D.=0.023, p=0.00002; *eif2b5*$^{zc103/zc103}$ normalized height: mean=0.551;
289 S.D.=0.018; *eif2b5*$^{+/+}$ normalized height: mean=0.629, S.D.=0.035, p=0.0006) **(Source-**
290 **Supplemental Figure 1)**. We also found a change in the intensity between the grey of the optic
291 tectum and the white matter of the periventricular grey zone in the T2 MRI images from the
292 rhombencephalic ventricle (RV) at the end of the midbrain moving rostrally (*eif2b5*$^{zc103/zc103}$
293 normalized intensity: mean=0.849; S.D.=0.108; *eif2b5*$^{+/+}$ normalized length: mean=0.743,
294 S.D.=0.091, p=0.0005) **(Figure 4I)**.
295

Figure 4. Adult *eif2b5* $^{zc103/zc103}$ mutants show myelin defects. A-C Transmission electron microscopy (TEM) of adult ei*f2b5*$^{zc103/zc103}$ optic nerve compared to ei*f2b5*$^{+/+}$ adults. Scale bar 2 µm. (A) ei*f2b5*$^{+/+}$ adult TEM image. (B) ei*f2b5*$^{zc103/zc103}$ adult TEM image. (C-E). Comparison of ratio between axon perimeter and myelin sheath perimeter, G-ratio, between ei*f2b5*$^{zc103/zc103}$ and ei*f2b5*$^{+/+}$; axon diameter and myelin thickness quantification shown. (F-G) Black Gold stain of adult ei*f2b5*$^{zc103/zc103}$ optic tectum compared to ei*f2b5*$^{+/+}$ adults. Scale bar 5 µm. (F) ei*f2b5*$^{+/+}$ adult Black Gold stained image. (G) ei*f2b5*$^{zc103/zc103}$ adult Black Gold stained image. (H-J) Magnetic Resonance Image (MRI) of adult ei*f2b5*$^{zc103/zc103}$ compared to ei*f2b5*$^{+/+}$. Scale bar 2 mm. Slice scheme of MRI images from the rhombencephalic ventricle (RV) at the end of the midbrain moving rostrally. (G) ei*f2b5*$^{+/+}$ adult T2 MRI image slice 1. (H) ei*f2b5*$^{zc103/zc103}$ adult T2 MRI of slice 1. (I) T2 intensity analysis. The normalized change in intensity from the from grey matter region of the optic tectum to the white matter region of the periventricular grey zone of the optic tectum, indicated by red boxes.

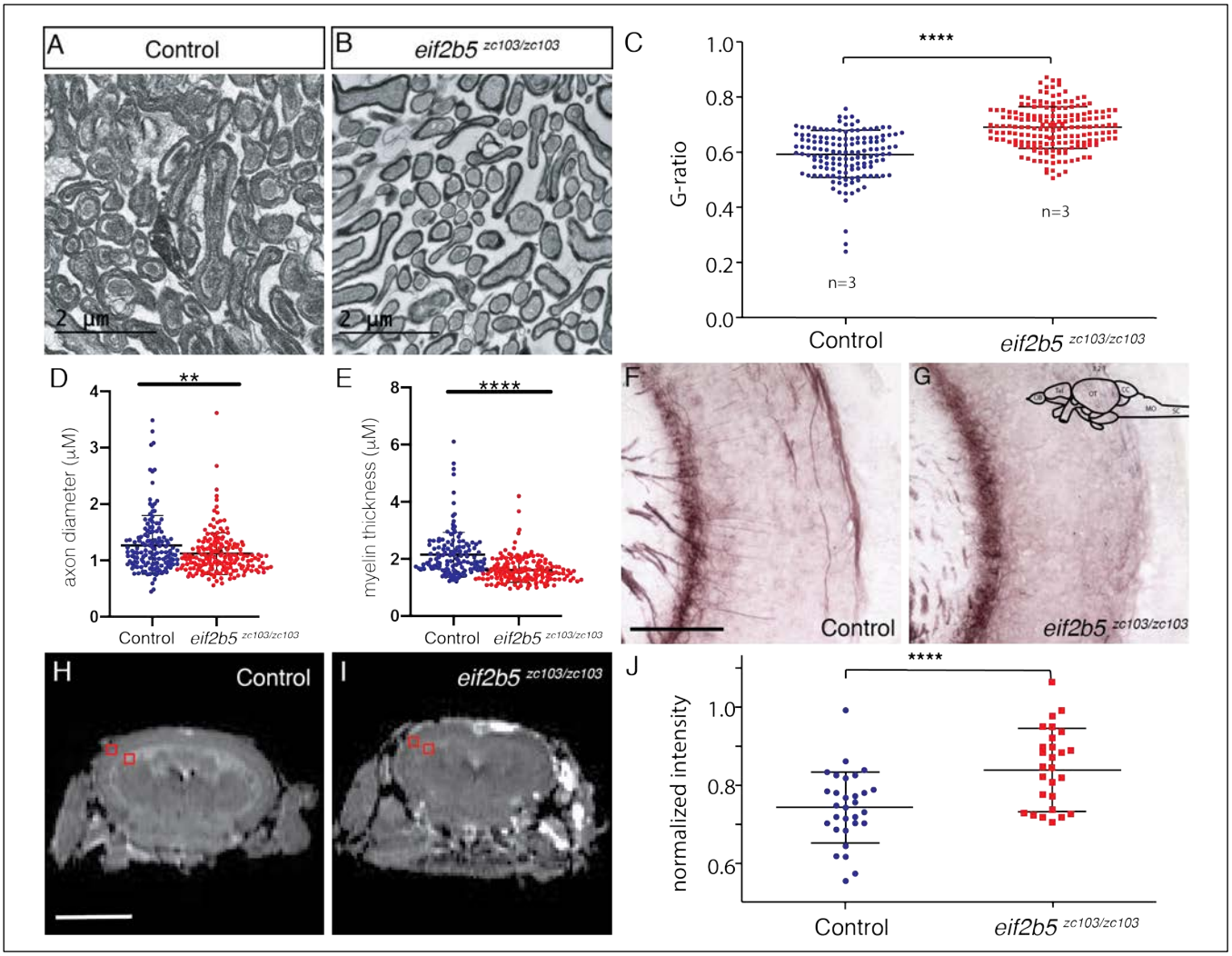

Figure 4- Source Data 1: Quantification of TEM results.

Figure 4- Source Data – Supplemental Figure 1. MRI images of adult wild-type control siblings and *eif2b5*$^{zc103/zc103}$ fish, showing decreased head and body size.

313 **Human *EIF2B* genes rescue zebrafish *eif2b* mutant lethality and CNS apoptosis**

314 Although the human and zebrafish *eif2b* subunit genes show significant conservation in
315 protein sequence, an important question for modeling VWM is to demonstrate functional
316 conservation. Zebrafish and human *eif2b2* ortholog amino acids are highly conserved, and
317 both orthologs have the same number of exons **(Figure 5A-C)**. To test functional conservation,
318 we created transgenic animals ubiquitously expressing human *EIF2B2*. We created a Tol2
319 transposable vector in which the human *EIF2B2* gene and enhanced green fluorescent protein
320 (eGFP) was expressed under control of the ubiquitously-expressing promoter ß-actin **(Figure**
321 **5D)**. We mated *eif2b2*$^{sa177223/+}$ heterozygous adults, and injected their embryos at the one cell
322 stage with the human *EIF2B2* vector to introduce the transgene (Tg) into the germline.
323 Embryos were screened at 3 dpf, and those positive for GFP were grown up to adults and
324 genotyped **(Figure 5G)**. The transgenic mutant *eif2b2*$^{sa177223/\,sa177223}$;Tg(*ß-actin:EIF2B2-2A-*
325 *EGFP*) larva developed a swim bladder and the growth deficits were rescued **(Figure 5F).** As
326 adults, the GFP positive *eif2b2*$^{sa177223/+}$;Tg(*ß-actin:EIF2B2-2A-EGFP*) were crossed with non-
327 transgenic *eif2b2*$^{sa177223/+}$. The offspring from this cross were genotyped and compared to a
328 non-transgenic *eif2b2*$^{sa177223/+}$ in-cross. Typically, *eif2b2*$^{sa177223/\,sa177223}$ have early lethality by
329 10 dpf. In contrast the transgenic homozygous mutant *eif2b2*$^{sa177223/\,sa177223}$;Tg(*ß-*
330 *actin:EIF2B2-2A-EGFP*) animals showed 21% survival at 10 dpf (e.g. Mendelian ratios)
331 **(Figure 5E)**. This increase in transgenic homozygous mutant survival continued to adulthood,
332 and the mutants were able to mate and were fertile. Further, the *eif2b2*$^{sa177223/sa177223}$ increase in
333 apoptosis **(Figure 5H-I, L)** was rescued and apoptosis in the *eif2b2*$^{sa177223/sa177223}$;Tg(*ß-*
334 *actin:EIF2B2-2A-EGFP*) was significantly reduced (TUNEL counts *eif2b2*$^{sa17223/sa17223}$

335 transgenic: mean=31.5, S.D.=12.9; *eif2b2*$^{sa17223/sa17223}$ non-transgenic: mean=84.4, S.D.=27.63,

336 p=1.89E-05) **(Figure 5J-L)**.

337 **Figure 5.**

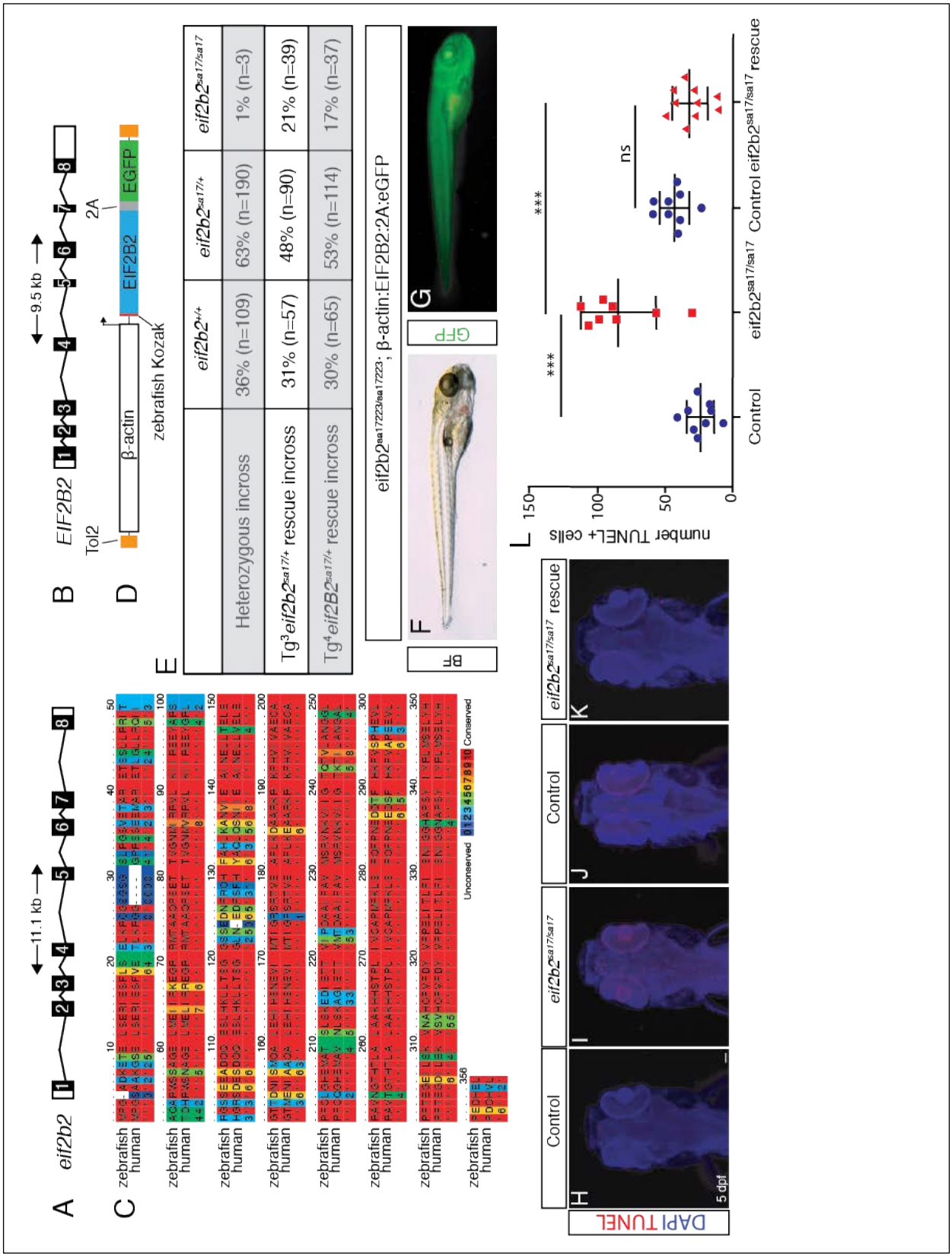

Figure 5. Human *EIF2B2* gene rescues zebrafish *eif2b2*$^{sa17223/sa17223}$ mutants. (A) 11.1 kb zebrafish *eif2b2* gene structure. (B) 9.5 kb human *EIF2B2* gene structure. (C) Conservation of amino acid sequence between zebrafish *eif2b2* and human *EIF2B2.* (D) Schematic of rescue construct containing Tol2, β-actin, human *EIF2B2,* and eGFP. (E) Genotype results (at adult age), of an *eif2b2*$^{sa17223/+}$ heterozygous incross, and an *eif2b2*$^{sa17223/+}$ heterozygous zebrafish crossed with two different transgenic alleles (#3 and #4): *eif2b2*$^{sa17223/+}$;Tg^{3}(*β-actin:EIF2B2:2A:eGFP*) or *eif2b2*$^{sa17223/+}$;Tg^{4}(*β-actin:EIF2B2:2A:eGFP*) heterozygous zebrafish. (F) Bright-field image of *eif2b2*$^{sa17223/sa17223}$;*β-actin:EIF2B2:2A:eGFP* mutant fish containing a swim bladder and regular-sized head. (G) Immunofluorescent image of expression of GFP in *eif2b2*$^{sa17223/sa17223}$;*β-actin:EIF2B2:2A:eGFP* mutant fish. (H-K) TUNEL and DAPI antibody staining of wild-type control; e*if2b2*$^{sa17223/sa17223}$ mutant; *eif2b2*$^{+/+}$;*β-actin:EIF2B2:2A:eGFP* wild-type control; and *eif2b2*$^{sa17223/sa17223}$;*β-actin:EIF2B2:2A:eGFP* mutant. (L) Quantification of TUNEL+ cells.
Figure 5- Source Data 1: Quantification of TUNEL results.

eif2b mutants express a truncated *eif2b5* transcript that causes ISR activation and defects in behavior

Work studying cancer cell lines has shown that during periods of hypoxia, ISR activation leads to retention of intron 12 in *EIF2B5* by interfering with the exon 12 splice site (Brady et al., 2017) (**Figure 6A**). This retained intron contains a premature stop codon, resulting in a truncated 65 kDa EIF2B5 protein, and rendering the eIF2B complex unable to initiate translation. To test whether the ISR in VWM could similarly affect *eif2b5* splicing, we tested intron 12 retention. We found an increase in retention of intron 12 associated with truncated *eif2b5* in *eif2b* mutant alleles (*eif2b5*: *zc102* and *zc103; eif2b2*: *sa17223*) (**Figure 6B**); and which was also observed in peripheral lymphocytes from a human VWM patient (**Figure 6C**).

To test whether the 65kDa EIF2B5 has a dominant-negative effect, we expressed a truncated *eif2b5* in wild-type embryos, and found impairment of motor behavior (**Figure 6D**). Since in VWM chronic activation of the ISR is believed to contribute to pathophysiology, we

368 examined ISR activation in *eif2b5* mutants by analyzing the expression of *atf4*, a key regulator
369 in ISR. qRT-PCR analysis showed *atf4* expression was increased in *eif2b5* mutants (**Figure**
370 **6E),** indicating that at baseline in the zebrafish mutants there was ISR activation. Next, we

371 also examined ISR activation in wild-type embryos expressing truncated *eif2b5*. qRT-PCR

372 showed that ISR markers including *atf4*, *chop II*, *bip* and *perk*, were up-regulated (**Figure 6F**),

373 indicating that truncated *eif2b5* was sufficient to activate ISR.

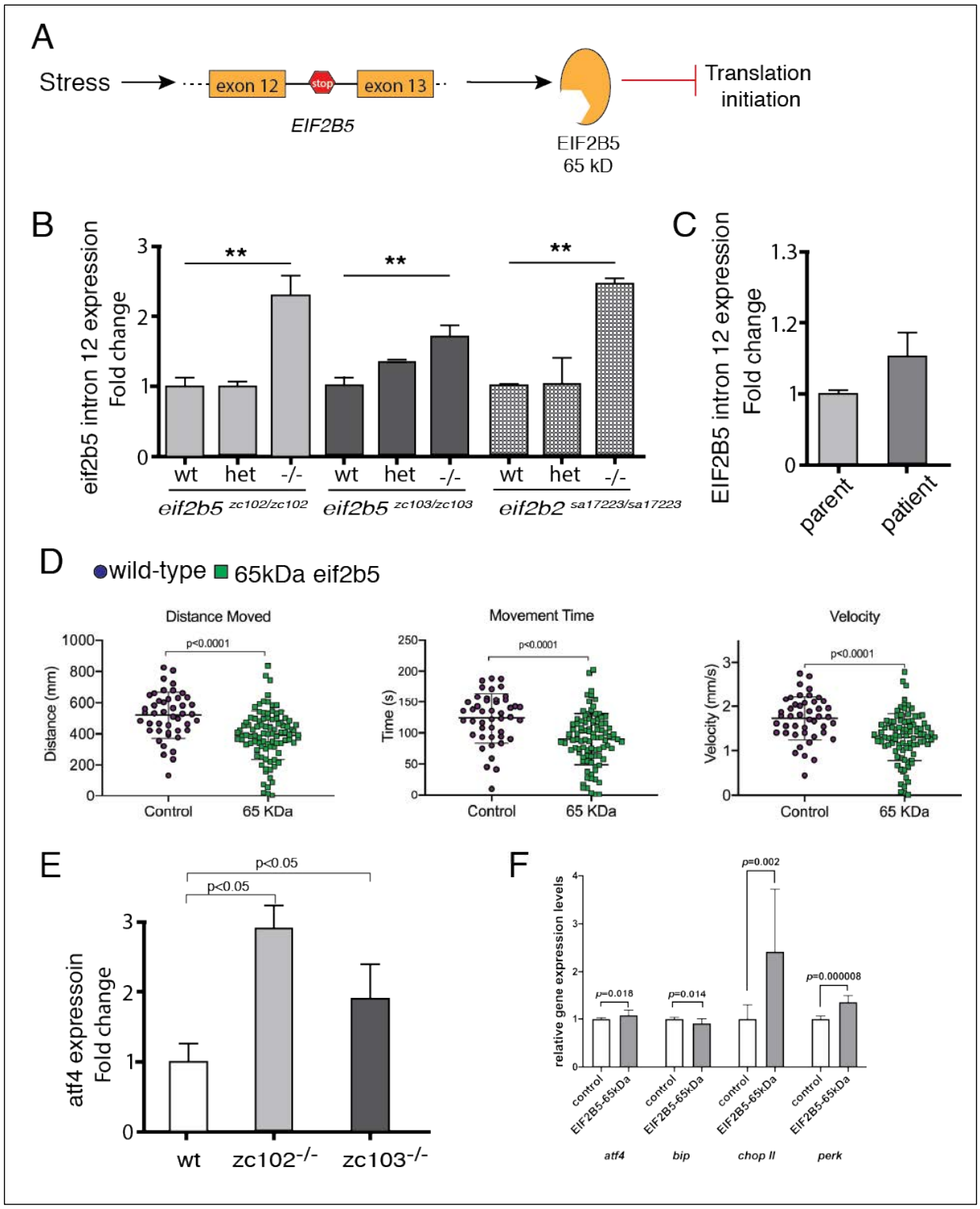

Figure 6.

Figure 6. Zebrafish *eif2b5* mutant alleles show intron retention, activated ISR, and role of truncated Eif2b5 in worsening phenotype. (A) Schematic showing integrated stress response activated intron 12 retention of *eif2b5* resulting in premature stop codon and truncated form of EIF2B5. (B) Fold change of *eif2b5* intron 12 expression with qRT-PCR in ei$f2b5^{zc103/zc103}$, $eif2b5^{zc102/zc102}$, and $eif2b2^{sa17223/sa17223}$ mutants relative to controls. (C) qRT-PCR for intron 12 expression in a VWM patient and their control unaffected father. (D) Control-injected larvae, compared to those injected with truncated *eif2b5* construct, shows impaired swimming behavior; distance moved, time spent moving, and velocity, at 5 dpf. (E) qRT-PCR for *atf4* ISR transcript shows increased expression in *eif2b5* mutants zc102 and zc103. (F) qRT-PCR for ISR transcripts (*atf 4*, *bip*, *chop II*, and *perk*) shows increased expression following injection of truncated *eif2b5* construct.
Figure 6- Source data File 1: qRT-PCR for intron 12 expression changes (*eif2b5*, zebrafish).
Figure 6- Source data File 2: qRT-PCR for intron 12 expression changes (*eif2b2*, zebrafish).
Figure 6 – Source data File 3: qRT-PCR for intron 12 expression changes (human).
Figure 6- Source data File 4: Behavior data for truncated *eif2b5* effects.
Figure 6- Source data File 5: qRT-PCR for *atf4* expression.
Figure 6- Source data File 6: qRT-PCR for ISR transcripts expression changes following injection with truncated *eif2b5*.

Discussion

We have generated and characterized a zebrafish model for VWM by analysis of alleles in *eif2b1*, *2, 4*; and an allelic series in *eif2b5*. The zebrafish *eif2b* mutants phenocopy important aspects of human VWM, including increased morbidity and mortality, altered myelination, and impaired motor behavior. Further, using rescue with expression of the human *EIF2B2* cDNA, we demonstrate functional conservation in the zebrafish *eif2b2* mutant. Importantly, our data reveals a novel potential mechanism of VWM pathophysiology: ISR activation in the *eif2b* mutants causes abnormal splicing and generation of a truncated *eif2b5* transcript, which is capable of further activating the ISR and impairing motor behavior. Thus, in healthy individuals, stress would activate the ISR but would appropriately be terminated through down-regulation of the ISR by dephosphorylation of eIF2 (Pakos-Zebrucka et al., 2016). But in VWM patients, stress would activate the ISR, and would also lead to expression of truncated *EIF2B5* expression;

406 which would cause a feed-forward mechanism of further and chronic ISR activation (**Figure 7).**

407 This chronic activation of the ISR is observed in human autopsy samples and in a mouse VWM

408 model (van der Voorn et al., 2005; van Kollenburg et al., 2006; Wong et al., 2019).

409

410 **Figure 7.** Feed-forward effect of truncated EIF2B5. A-C) Under normal conditions, stress leads
411 to activation of the ISR, which is terminated by dephosphorylation of eIF2a by PP1 (protein

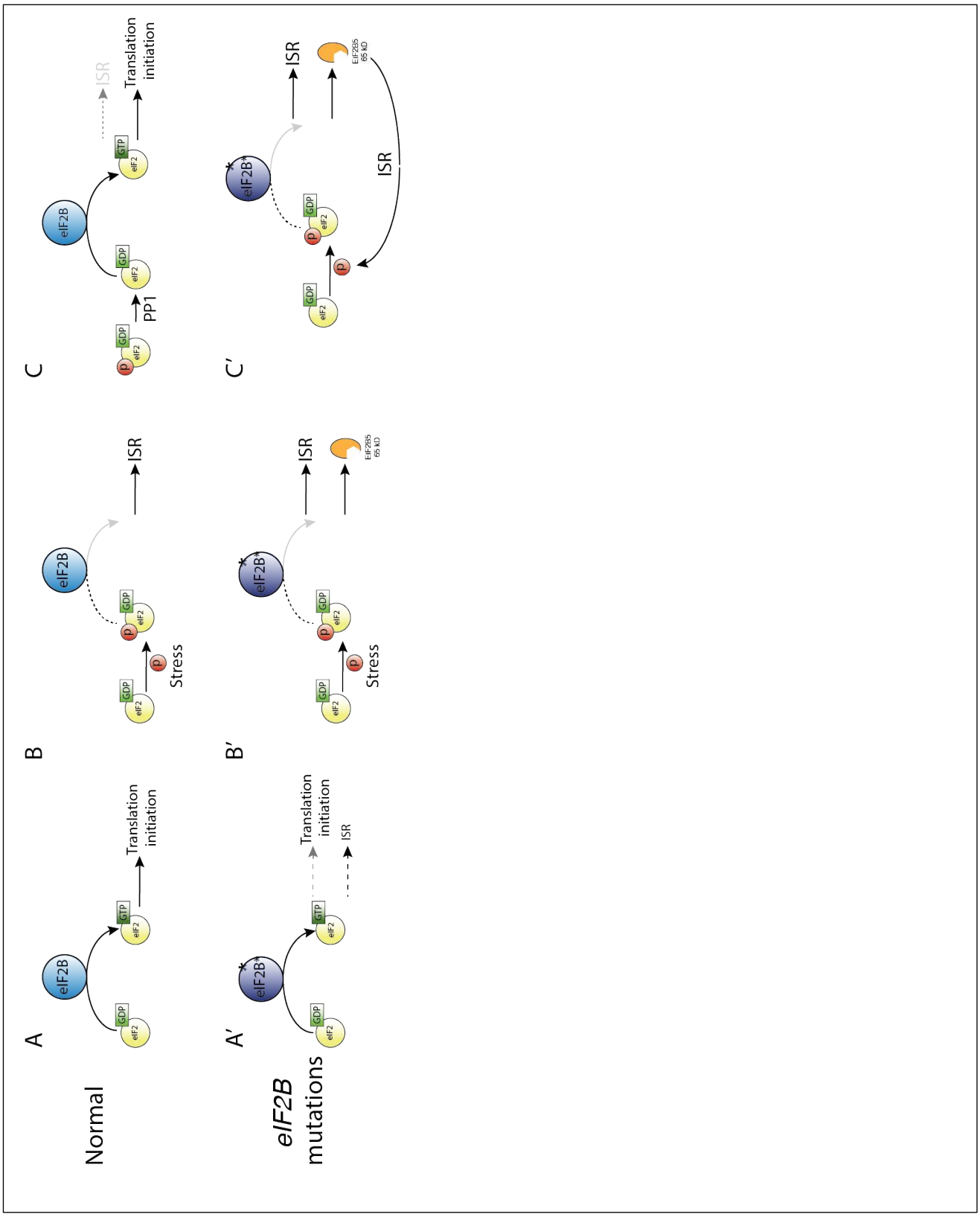

phosphatase 1 complex) and resumption of normal cap-dependent translation. A'-C') In the presence of *eif2b* subunit mutations in VWM, normal translation is impaired, and there is activation of the ISR above baseline (A'). In response to stress, there is ISR activation and expression of truncated EIF2B5, which leads to chronic activation of the ISR and an inability to terminate the ISR.

The eIF2B complex is comprised of five subunits that together act as the guanine nucleotide exchange factor for eIF2, governing the rate of global protein synthesis and cap-dependent translation initiation. VWM can be caused by autosomal recessive mutations in any of the five subunits of eIF2B. Zebrafish show expression of the *eif2b* genes at 24 hpf through 7 dpf including in the CNS. Mutations in the most commonly affected patient subunits, *eif2b2* and *eif2b5,* showed growth deficits and decreased survival, mimicking clinical features of VWM. Since we found that human *EIF2B2* expression in zebrafish can rescue the increased apoptosis and early lethality phenotype of *eif2b2* ^{sa17223} homozygous mutants, our work suggests conservation of *eif2b* expression and function.

Mutations in the zebrafish eIF2B complex were associated with multiple defects in development of the CNS. In the 5 dpf homozygous mutants of *eif2b2*^{sa17223}, *eif2b5*^{zc102} and *eif2b5*^{zc103} alleles there was an increase in apoptosis in the CNS. We also observed altered patterns of cell proliferation pattern in the CNS, and a decrease in overall CNS proliferation in the *eif2b2*^{sa17223} mutants. Although there was no change in total oligodendrocyte precursor cell numbers in the spinal cord or brain, we found an increase in the number of oligodendrocyte precursor cells undergoing apoptosis in the hindbrain. We also observed impaired myelination, marked by a decrease in thickness of the myelin sheath, abnormal patterning of myelinated axon tracts in the optic tectum, and abnormal intensity of white matter regions on MRI.

Since a hallmark of VWM is that disease progression can be precipitated by stressors, we tested the ISR and the response to stress in the *eif2b* mutants. We noted that while stress of wild

type zebrafish caused motor deficits, stress in the mutant *eif2b* zebrafish (including heat shock, hypoxia, or thapsigargin) did not worsen further worsen their already impaired motor behavior (data not shown). This suggests that the *eif2b* mutant zebrafish are already "maximally" stressed at baseline, consistent with the observed activation of the ISR at baseline, and the finding of increased intron 12 retention. ISR induces expression of transcription factors including ATF4 (Harding et al., 2000; Watatani et al., 2008). ATF4 and other components of the ISR trigger a stress-induced transcriptional program that promotes cell survival during mild or acute conditions, but which causes pathological changes under severe or chronic insults (Pakos-Zebrucka et al., 2016).

A poorly understood aspect of VWM is why a minor stressor can precipitate significant white matter loss and neurological deterioration. Our work suggests that this is caused by a feed-forward effect of chronic ISR that cannot be terminated. This occurs by alternative splicing and retention of intron 12 in *eIF2B5* leading to a premature stop codon and expression of a truncated eIF2B5. This was first observed in cancer cell lines in response to hypoxia (Brady et al., 2017). We showed that truncated *eif2b5* is expressed in VWM mutants, and that expression of the truncated *eif2b5* impairs motor function, and itself leads to further activation of the ISR.

Major advances in the past several years have shown that a small molecule stabilizing the decameric eIF2B complex (ISRIB - ISR inhibitor) can boost the GEF activity of wild-type and VWM mutant eIF2B complexes (Tsai et al., 2018; Wong et al., 2018) and can inhibit the ISR in mice bearing an $Eif2b5^{R132H/R132H}$ VWM mutation (Wong et al., 2019). However, it is not clear whether ISRIB or other drugs targeting eIF2B complex stability will be sufficient to prevent stress-induced ISR chronic, feed-forward activation. Therapies for VWM may need a

combinatorial approach incorporating eIF2B stabilization at baseline; and prevention of stress-induced truncated eIF2B5 expression.

Methods

Ethics Statement

Zebrafish experiments were performed in strict accordance of guidelines from the University of Utah Institutional Animal Care and Use Committee (IACUC), regulated under federal law (the Animal Welfare Act and Public Health Services Regulation Act) by the U.S. Department of Agriculture (USDA) and the Office of Laboratory Animal Welfare at the NIH, and accredited by the Association for Assessment and Accreditation of Laboratory Care International (AAALAC).

Human subjects-related aspects of the study were approved by the Institutional Review Board of the University of Utah and the Privacy Board of Intermountain Healthcare.

Fish stocks and embryo raising

Adult fish were bred according to standard methods. Embryos were raised at 28.5°C in E3 embryo medium and staged by time and morphology. For *in situ* staining and immunohistochemistry, embryos were fixed in 4% paraformaldehyde (PFA) in 1xPBS overnight (O/N) at 4°C, washed briefly in 1xPBS with 0.1% Tween-20, serially dehydrated, and stored in 100% MeOH at -20°C until use. Transgenic fish lines and alleles used in this paper were the following: Tg(*olig2:dsRed)*^{vu19} (Kucenas et al., 2008) and Tg(*sox10:mRFP*) (Park et al., 2005).

eif2B Sequence Analysis

Human and zebrafish *eif2b1*, *eif2b2*, *eif2b3*, *eif2b4* and *eif2b5* subunit genes amino acid sequences were compared using Clustal Omega (https://www.ebi.ac.uk/Tools/msa/clustalo/) (Sievers et al., 2011) and aligned using PRALINE (http://www.ibi.vu.nl/programs/pralinewww/) (Simossis and Heringa, 2005); phylogenetic tree analysis was performed with Phylodendron (http://iubio.bio.indiana.edu/treeapp/treeprint-form.html).

Zebrafish *eif2b* mutant lines obtained from Sanger Zebrafish Mutation Project

We obtained the *eif2b1*^{sa12357}, *eif2b2*^{sa17223}, *and eif2b4*^{sa17367} alleles generated by the Sanger Zebrafish Mutation Project per our request and established these lines as viable stock at our facility. The *eif2b1*^{sa12357} allele results in a T>A nonsense mutation resulting in an early stop in exon 8. The *eif2b2*^{sa17223} and *eif2b4*^{sa17367} alleles have mutations in an essential splice site predicted to interrupt splicing from exon 5 to 6 of *eif2b2* by a G>A mutation at the end of exon 5 (744 nt), and from exon 12 to 13 in *eif2b4* by a G>A mutation at the end of exon 12 (1404 nt).

***eif2b5* CRISPR sgRNA construction and injection**

Targeting the *D. rerio eif2b5* gene (Ensembl Zv10: ENSDART00000110416.4) for CRISPR mutagenesis was performed by the University of Utah Mutation Generation and Detection Core (http://cores.utah.edu/mutation-generation-detection/). We designed sgRNA target sites by looking for sequences corresponding to $N_{18}GG$ on the sense or antisense strand of the DNA using the CRISPR design program at http://crispr.mit.edu. Off-target effects were checked through the use of NIH BLAST tool applied to the zebrafish genome (zv10). Off-target sequences that had significant matches of the final 23 nt of the target and NGG PAM sequence were discarded.

sgRNAs targeting exon 1 (*eif2b5*-ex1) were transcribed using DraI-digested gRNA expression vectors as templates, and the HiScribe T7 RNA Synthesis kit (New England BioLabs) followed by RNA purification with Micro Bio-spin 6 columns (BioRad).

To maximize mutagenesis and minimize lethality, an *eif2b5-ex1* sgRNA dose curve was performed. A mix of *eif2b5-ex1* sgRNA (between 250 pg-600 pg) and Cas9 protein (600 pg, Integrated DNA Technologies) were injected into one cell stage embryos, as previously described. CRISPR efficiency was evaluated on individual 24 hpf injected embryos after DNA extraction, PCR amplification of the target locus, and HRMA analysis. An *eif2b5-ex1* sgRNA dose of 450 pg resulted in >90% mutagenesis in 24 hpf embryos, assayed by HRMA, with no difference in survivability compared to uninjected controls. Embryos used for injection were derived from wild-type AB parents, previously confirmed at the *eif2b5* locus to have exact homology for the sgRNA sequence.

HRMA PCR

DNA was extracted from embryos (24 hpf-72 hpf), or fin clips from adults, into 50mM NaOH, and incubated at 95˚C for 20 min, followed by neutralization with 1M Tris pH 8.0 (1:10 by volume) as previously described (Xing et al., 2014). Oligonucleotides were designed using Primer3 (https://www.ncbi.nlm.nih.gov/tools/primer-blast/) to give 60-100 nucleotide products spanning the CRISPR cleavage site, and tested *in silico* using uMELT (https://www.dna.utah.edu/umelt/umelt.html) to determine PCR products with optimal thermodynamic profiles. PCR was performed using LightScanner Master Mix System (BioFire) in 10 µl reactions as previously described (Xing et al., 2014). Thermal melt profiles were collected on a LightScanner (Idaho Technology) (65-98 C, hold 62˚ C) and analyzed with LightScanner Software.

Genotyping was performed by PCR and high-resolution melt analysis (HRMA), using the LightScanner Master Mix system. For *eif2b5* alleles with mutations in exon 1, we used the following primers and conditions: (*eif2b5* forward primer) 5'-AAGCCGGTGTCGGATAAAGAT-3' and (*eif2b5* reverse primer) 5'-AAACCTGCGGTTGAAACTGTC-3'; 95˚C for 2 min, followed by 29 cycles of 94˚C for 30 s, and 60˚C for 30 s, followed by a final denaturation and annealing step of 95˚C for 30 s, and 25˚C for 30 s. For *eif2b2*^{sa17223} genotyping we did PCR with the following primers and conditions: (*eif2b2* forward primer) 5'- TAATGTCACGAGTCAATAAG-3' and (*eif2b2* reverse primer) 5'-AGGATTAATCTTTTATTTCA-3'; 95˚C for 2 min, followed by 29 cycles of 94˚C for 30 s, and 60˚C for 30 s, followed by a final denaturation and annealing step of 95˚C for 30 s, and 25˚C for 30 s. For *eif2b4*^{sa17367} genotyping we did PCR with the following primers and conditions (*eif2b4* forward primer) 5'-TTGAGCATCAAAAGGGTTATTG -3' and (*eif2b4* reverse primer) 5'-CGGACTCTTTTGTATCCAATG -3'; 95˚C for 2 min, followed by 29 cycles of 94˚C for 30 s, and 55˚C for 30 s, followed by a final denaturation and annealing step of 95˚C for 30 s, and 25˚C for 30 s. All PCR was run in an optically transparent plate with 25 µl mineral oil overlay. We then performed HRMA to differentiate the *eif2b* melt-curves from their corresponding controls.

For *eif2b1*^{sa12357} genotyping, HRMA analysis was not able to reliably identify mutant versus wild-type alleles. We therefore used the restriction endonuclease sequence Hpy188I (taTCAGAtg) present in the wild-type allele of *eif2b1*, but not in the *eif2b1*^{sa12357} mutant allele (taACAGAtg) to create a restriction fragment length polymorphism (RFLP) for genotyping. We first performed PCR of the target locus (667bp) in a 10 µl reaction, with the following primers and conditions (*eif2b1* forward primer) 5'- GGAGACGTAAAATGTACCTGCAAT-3' and (*eif2b1* reverse primer) 5'-CACCCCAACCATCACAGGAG-3'; 98˚C for 1 m, followed by 34

cycles of 98˚C for 10s, 58˚C for 15s, and 72 for 25s, followed by a final extension step of 72˚C for 10m. Following PCR, the entire 10 µl reaction was digested with Hpy188I in a 15 µl reaction for 2hrs at 37˚C. The digest was then run out on a 2.5% agarose gel. Animals homozygous for *eif2b1*$^{sa12357/sa12357}$ produced a 623 bp mutant band, and a 44 bp band unrelated to the *eif2b1*^{sa12357} allele, used as an internal control for the restriction digest. Wild-type animals, harboring the non-mutated Hpy188I restriction site, generate a 404 bp and 219 bp band, specific to the wild-type allele, as well as the 44 bp internal control band; heterozygous animals generate all four bands after Hpy188I digestion: mutant 623 bp, wild-type 404 bp and 219 bp, and the internal digest control band 44 bp.

Chip Genotyping

Survival genotyping of 72 hpf zebrafish was performed as previously described (Lambert et al., 2018). Briefly, embryos were loaded individually onto genotyping wells of a ZEG chip (wFluidx, Inc.) in 12 µl of E3 with a wide bore pipette tip. Once embryos are loaded, the ZEG chip was placed on the vibration unit, covered with the lid and vibrated for 7.5 minutes at 1.4 volts, 0.026 amps and 0.03 watts. After the samples are vibrated, 10 µl of E3 is removed from the well into a PCR strip tube. The corresponding embryo is removed from the chip well with a transfer pipette and a small amount of E3, into a 96 square well plate (650 µl/well) until after genotyping. For genotyping PCR, 5 µl of E3 is removed from each well is used directly in the PCR without further cell lysis steps.

Cloning and characterization of zebrafish *eif2b5* CRISPR mutants

eif2b5-ex1 CRISPR injected F0 embryos were raised and crossed to non-mutagenized wild-type AB siblings. *eif2b5* F1 founder offspring were then raised to adulthood, fin-clipped for DNA extraction and PCR amplification of the target locus, using the above described HRMA

primers for *eif2b5*. Individual fish identified as potential mutants by HRMA were further confirmed by Topo-TA cloning (Thermo Fisher Scientific) of the target locus, and Sanger sequencing four clones per animal. To ensure that we did not miss larger mutations at the CRISPR mutagenesis site, PCR amplification of a larger region surrounding the target locus (517bp) was performed using the following primers and PCR conditions: (*eif2b5* forward sequencing primer) 5'- AGCTACCTCAACAGGGCGTA-3', and (*eif2b5* reverse sequencing primer) 5'- CGTCCAAAAACAAAACAGCA-3'; 98˚C for 1 m, followed by 34 cycles of 98˚C for 10s, 60˚C for 15s, and 72 for 20s, followed by a final extension step of 72˚C for 10m.

Cloning of Human *EIF2B2* and *EIF2B5*

Human *EIF2B2* and *EIF2B5* were amplified from cDNA prepared from SH-SY5Y human cell line. The following primers, and PCR conditions were used to amplify *EIF2B2* for cloning into a middle entry clone Gateway-compatible vector (*EIF2B2* forward primer contains: 31 nt *att*B1F sequence, a 9 nt zebrafish optimized Kozak sequence, and 20 nt region of *EIF2B2* beginning at the ATG) 5'-GGGGACAAGTTTGTACAAAAAAGCAGGCTACGCCGCCACCATGCCGGGATCCGCAGCGAA-3', and (*EIF2B2* reverse primer contains: 30 nt *att*B2R sequence, and a 20 nt region of the 3' *EIF2B2* that does not contain the stop codon) 5'-GGGGACCACTTTGTACAAGAAAGCTGGGTCTAAAACATGATCATCAGGAT-3'; PCR conditions: 98˚C for 1 m, followed by 34 cycles of 98˚C for 10s, 68˚C for 15s, and 72 for 30s, followed by a final extension step of 72˚C for 10m. The following primers, and PCR conditions were used to amplify *EIF2B5* for Gateway cloning (*EIF2B5* forward primer contains: 31 nt *att*B1F sequence to allow for Gateway pME cloning, a 9 nt zebrafish optimized Kozak sequence, and a 20 nt region of *EIF2B5* beginning at the ATG) 5'-

596 GGGGACAAGTTTGTACAAAAAAGCAGGCTACGCCGCCACCATGGCGGCCCCTGTAG
597 TGGC-3', and (*EIF2B5* Reverse primer contains: 30 nt *att*B2R sequence to allow for Gateway
598 pME cloning, and a 20 nt region of the 3' *EIF2B5* that does not contain the stop codon) 5'-
599 GGGGACCACTTTGTACAAGAAAGCTGGGTCTCAGTCATCTTCAGATGACT-3'; PCR
600 conditions: 98˚C for 1 m, followed by 34 cycles of 98˚C for 10s, 68˚C for 15s, and 72 for 75s,
601 followed by a final extension step of 72˚C for 10m.
602 The *att*B containing *EIF2B* PCR product were combined with a donor vector (pDonor
603 #221) in a BP recombination reaction to generate Gateway middle clones, pME *EIF2B2* and
604 pME *EIF2B5*. These plasmids were then diagnostically digested and sequenced to confirm the
605 correct cloning. Expression clones were assembled using the Tol2 kit and recombination
606 reactions with Gateway plasmids. For expression and visualization of human *EIF2B5* (pME
607 *EIF2B5*) in the zebrafish we used the ubiquitous *Beta actin* enhancer containing a minimal core
608 promoter (mcp) encoding the viral E1b TATA box fused to the carp b-actin 5' UTR (p5E *Beta*
609 *actin*) and the viral 2A bicistronic eGFP fluorescent tag (p3E *2A:eGFP*) assembled into the
610 pDestTol2pA2 plasmid.
611 **Immunohistochemistry and in situ hybridization**
612 Immunohistochemistry was performed as previously described (Bonkowsky et al., 2008).
613 Antibodies used were: mouse anti-acetylated tubulin 1:250 (Sigma), mouse monoclonal anti-
614 GFP 1:250 (Millipore), chicken anti-GFP 1:1000 (Aves Labs), mouse anti-HuC/D 1:400
615 (ThermoFisher), rabbit anti-dsRed 1:250 (Clontech), Cy-3 anti-rabbit 1:400 (Millipore), Alexa
616 488 donkey anti-mouse 1:400, Alexa 633 donkey anti-rabbit, Alexa 488 donkey anti-chicken
617 1:400, Alexa 555 rabbit anti-goat 1:400 (ThermoFisher), and 4',6-diamidino-2-phenylindole
618 (DAPI).

In situ *hybridization*

The antisense digoxigenin-labeled cRNA probes for zebrafish *eif2b1-5* were prepared by using a clone-free method, as previously described (Thisse and Thisse, 2008). Forward and reverse primers were generated using Primer3 to generate a PCR product between 800-950 nt. The following primers were used: *eif2b1* forward *in situ* primer 5'-CGTTGCATCAGCGACACTAT-3', *eif2b1* reverse *in situ* primer 5'-GAAATGCTTTATAAACAGCAATAATCA-3'; *eif2b2* forward *in situ* primer 5'-CGCAGGTGAACTGATGGAG-3', *eif2b2* reverse *in situ* primer 5'-GATGTTTTGAATGCCAGACG-3'; *eif2b3* forward *in situ* primer 5'-GAGAACAGCGGGACTTTGTC-3', *eif2b3* reverse *in situ* primer 5'-TTCGTCTTCAGGCCTGTTCT-3',; *eif2b4* forward *in situ* primer 5'-GGATCCAATGCTCGATCTGT-3', *eif2b4* reverse *in situ* primer 5'-GAGGGAAGTGTGTGCATCTG-3'; *eif2b5* forward *in situ* primer 5'-TGGTGGTGGGTCCAGATATT-3', *eif2b5* reverse *in situ* primer 5'-CAGCCCGTTGTATTTTCCAG-3'. To generate a PCR product for antisense probe generation, the reverse primer also contains a 32 nt sequence containing; a 9 nt 5' spacer sequence, a 17 nt T7 polymerase sequence, and a 6 nt 3' spacer (5'-CCAAGCTTCTAATACGACTCACTATAGGGAGA -3'), resulting in a PCR product <1kb. Synthesis of digoxigenin-labeled antisense RNA probes were synthesized using a DIG RNA Labeling Kit (SP6/T7; Roche).

Microscopy and image analysis

Immunostained embryos were transferred step-wise into 80% glycerol/20% PBST, mounted on a glass slide with a #0 coverslip, and imaged on a confocal microscope. Confocal stacks were projected in ImageJ, and images composed with Adobe Photoshop and Illustrator.

TUNEL quantification

Terminal deoxynucleotidyl transferase dUTP nick-end labeling (TUNEL) was performed on whole-mount larvae (ApopTag Fluorescein *In Situ* Apoptosis Detection Kit; Millipore) as previously described (Lambert et al., 2012). Confocal imaging was performed and images were rendered in ImageJ by compiling a max sum projection of 100 µm (step size 2.5 µm) into a single z-stack image, for cell counting using Photoshop's (Adobe) count tool.

RNA isolation and cDNA synthesis

RNA was isolated from between 50-100 embryos per sample, depending on age. Each sample was suspended in 900 µl Trizol Reagent (Invitrogen), triturated with a 25-gauge needle until homogeneous; 270 µl chloroform was added and the sample was centrifuged for 15 m at 4 ˚C. The aqueous solution was moved to a new tube, an equal volume isopropanol (approximately 500 µl) was added, and 5 µl Glycoblue (Invitrogen) added, followed by centrifugation for 15 m at 4 ˚C. The pellet was washed in 70% ethanol, centrifuged for 10 m at 4 ˚C, and resuspended in 44 µl DEPC H_2O. To remove DNA, 5 µl DNase I buffer and 1 µl Turbo DNase (Invitrogen) was added to each sample and incubate for 15 m at 25˚C. The volume was brought to 400 µl with DEPC H_2O, and an equal volume phenol:chloroform was added, mixed, and centrifuged for 15 m at 4˚C. The aqueous phase was transferred to a new tube and 1.5 µl Glycoblue was added, 1/10 volume 3M NaOAc added, and 2.5x of the total volume of 100% ethanol was added. The sample was allowed to precipitate overnight at -20 ˚C. The sample was then centrifuged for 15 m at 4 ˚C, supernatant removed, and the pellet washed in 70% ethanol. This was followed by a final

centrifugation step of 15 m at 4 ˚C, supernatant removed, and the RNA resuspended in 15 µl DEPC H_2O.

First-strand cDNA was made from 1-5 µg total RNA using the SuperScript III First-Strand Synthesis System (Applied Biosystems) per manufacturer's instructions.

qRT-PCR

All qRT-PCR reactions were performed using SYBR Green PCR master mix (Invitrogen) and 2 µl cDNA with the following conditions: 50˚C for 2 min, 95 for 10 min followed by 39 cycles of 95˚C for 20s, 60˚C for 20s, and 72 for 20s, followed by a final melt curve step that ramps in temperature between 60˚C and 95˚C.

Behavior Analysis

Larval behavior analysis was performed on 7 dpf larvae in 96-well square bottom plates (Krackeler Scientific) using video analysis software (Noldus EthoVision). For spontaneous behavior, animals were transferred at 6 dpf to the 96-well plate and kept at 28.5˚C overnight. At 7 dpf the plate was placed on the video imaging system and animals were allowed to adapt in the dark for 10 min, and then recording was performed for 5 m (1 min dark and 4 min light).

TEM

Following fixation overnight at 4˚C (in 2.5% glutaraldehyde; 1% PFA in 0.1M sodium cacodylate, 8mM $CaCl_2$, 2.4% sucrose; pH 7.4), then processed and embedded in plastic as follows: rinsed 2 X ten minutes in 0.1M sodium cacodylate buffer containing 2.4% sucrose and 8mM $CaCl_2$. Tissue was then post-fixed in 2% osmium tetroxide in a 0.1M sodium cacodylate buffer for 1 hour at room temperature, followed by a rinse for 5 minutes in water filtered through a 0.22µm millipore filter. Staining was performed *en bloc* for 1 hour at room temperature with

saturated aqueous uranyl acetate, that was filtered through a 0.22µm millipore filter. Samples were dehydrated through a graded series of ethanol, 10 minutes at each step at room temperature. Tissue was then transitioned through three changes of absolute acetone, 10 min each, followed by infiltration with with increasing concentrations of plastic (Embed 812) as follows: 1hr, Plastic:Acetone 1:1; overnight, Plastic:Acetone 3:1, done at room temperature. Final plastic infiltration was carried out the following day by changing the plastic three times, then placing tissue vials on a rotator for 1hr and then under vacuum for 1hr. After the third change tissue was embedded in a fresh plastic in mold with appropriate labels and placed in 60-70˚C oven overnight. Once the plastic was cured the samples were thick sectioned (0.5-1.0um) and placed on glass slides; stained with 1% Toluidine Blue-O in 1% borax on a hot plate. Tissue was sectioned with a diamond knife on a Leica EMUC6 ultramicrotome, picked up on 150 mesh copper grids and contrasted sequentially with saturated aqueous uranyl acetate followed by staining with Reynold's lead citrate. Sections were examined on a JEOL 1400+ electron microscope.

MRI

The brains of wild-type (n=6; 7 months old) and *eif2b5*^{zc103} fish (n=6; 5.5 months old) were dissected leaving the skull, a small piece of the spinal cord, and a small amount of fat tissue surrounding the brain intact. They were placed in 4% paraformaldehyde and 0.5% magnevist (gadopentetate dimeglumine) overnight at 4˚C on a nutator.

MR imaging was performed with a 1.0cm diameter loop-gap radiofrequency transmitter-receiver and a preclinical 7T MRI scanner (Bruker Biospec) with the microimaging gradient set (1100mTm^{-1}, BGA-6, Bruker). Two primary scans were done to map the T1 and T2 behavior of the tissue. These scans were 3D turbo spin-echo scans (Rapid Acquisition with Refocused

Echoes, RARE), specialized with varying repetition time (TR) or echo time (TE) to optimize T1 and T2 contrast. The T1 map scan utilized the following parameters: T1 weighted RARE: TR = [50, 150, 275, 450, 600]ms, TE = 12ms, 4 averages, RARE factor = 2, matrix size = 305 x 140 x 165, spatial resolution = 0.036 mm isotropic, field of view: 110mm x 50mm x 60 mm. T2 weighted RARE: TR = 500ms, TE = [12.2, 36.6, 60.94]ms, 9 averages, RARE factor = 2, matrix size = 305 x 140 x 165, spatial resolution = 0.036 mm isotropic, field of view: 110mm x 50mm x 60 mm. Six zebrafish skulls were scanned in wild type/mutant pairs in the custom coil.

The raw intensity data was exported from Paravision 5.1 (Bruker BioSpec). This data was imported into MATLAB r2017b (Mathworks, Natick MA), and reshaped into two sets of 3D volumes. For the T1 weighted scan, each volume was representative of an individual TR. For the T2 weighted scans, each volume was representative of a different TE. With this, a gradient descent algorithm could be applied to the intensity vs TR, TE curve of each pixel, for the T1, T2 volumes respectively. General parameters were T1: Initial constants: M0 = 8000, T1 =150, Loop limit = 75000, learning rate=0.000001. Equation: $S = M_0(1 - e^{TR/T1})$ T2: Initial constants: M0 = 8000, T2 =75, Loop limit = 75000, learning rate=0.000001. Equation: $S = M_0 e^{TE/T2}$ Sub-millimeter movement was witnessed between the T1 experiments, which caused pixel intensities to not properly fit to the T1 equation, and blurred in the averaged image. This was corrected for with simple 2D rigid body transformations between TR experiments, using the MATLAB r2017b “affine2d” function. A transformation matrix was generated for a single representative slice, then applied to all slices within the volume. This transformation was applied to each T1 experiment of a given set and were averaged into a single volume.

Transformations matrices were generated with landmark based analysis. Three primary landmarks were utilized to build the transformation: the center of the lens of each eye and the tip

731 of the vagal lobe. The repetitions were averaged and fitted with the gradient descent algorithm
732 detailed above. This resulted in two volumes of T1 and T2 values for each scan pair. The skull
733 pair was separated into two distinct volumes for each T1, T2 map, and rotated into the
734 anatomical planes for visualization.

735 Analysis of the T1 and T2 maps involved a two-step process of quantifying overall brain
736 volume, and determining the T1 and T2 values for white matter regions of interest (ROI). To
737 begin, four representative measurements were taken for each wild type and mutant pair.
738 Measurements taken were the length from the tip of olfactory bulb to end of the tectum, the
739 maximum width of the optic tectum, and the maximum height of brain at center ventricle. These
740 measurements were normalized to the width of the specimen's skull.

741 To measure the intensity of white matter regions in the T2 images, a 2x2 pixel region was
742 taken from the periventricular grey zone and normalized to a 2x2 pixel region in the optic tectum
743 from a slice at the end of the rhombencephalic ventricle (RV) of midbrain. Two more slices
744 were measured moving rostrally from the RV.

745 **Black/Gold Staining**

746 Adult brains were dissected, fixed overnight in 4% PFA, then incubated 1 hr in 5%
747 sucrose in PBS, overnight in 15% sucrose in PBS, and overnight in 30% sucrose in PBS, prior to
748 embedding in OCT. Tissues were sectioned at 30µm at -20˚C in the cryostat and mounted on
749 positively charged slides.

750 Black Gold II powder (Millipore) was resuspended in 0.9% NaCl to a final concentration
751 of 0.3% and preheated to 60°C along with 1% sodium thiosulfate. Tissue sections were brought
752 to room temperature for 5 minutes, then post-fixed in 10% formalin for 1 hr. Slides were
753 incubated at 60°C in the pre-warmed Black Gold II solution for 15 minutes. Slides were rinsed

754 1X in tap water for 2 minutes, then incubated in sodium thiosulfate solution (1%) for 3 minutes
755 at 60°C. After another tap water rinse, slides were dehydrated to 100% EtOH, incubated in 50:50
756 Hemo-De:EtOH for 3 min, and finally in Hemo-De for 3 min prior to mounting in Cytoseal 60.

757 **Statistical Analysis and Blinding**

758 Statistical analyses were performed using Prism6 software (GraphPad). Student's *t*-test
759 was used for two-way comparisons; comparisons between three or more groups was performed
760 with ANOVA with post-hoc Tukey's HSD between individual means.

761 Samples were randomly allocated to control or experimental groups, other than required
762 distribution by genotype (e.g. wild-type embryos were in the wild-type group). Allocation of
763 samples and animals, data collection, and analysis were performed blinded to genotype and/or
764 experimental group.

765

Acknowledgements

Electron microscopy was performed at the University of Utah Electron Microscopy Core Laboratory with assistance from N. Chandler and D. Belnap. Confocal imaging was performed at the University of Utah Fluorescence Microscopy Core Facility, supported in part by an NCRR Shared Equipment Grant # 1S10RR024761-01. The University of Utah Centralized Zebrafish Animal Resource (CZAR) provided zebrafish husbandry, and is supported in part by NIH grant # 1G20OD018369-01. Sequencing was performed at the University of Utah DNA Sequencing Core Facility. CRISPR design and construction was performed at the University of Utah Mutation Generation and Detection Core.

Funding

This work was supported by the National Institutes of Health [grant number R21NS109441]; the Bray Chair in Child Neurology Research at the University of Utah; and the Brain and Spine Center of Primary Children's Hospital.

Declaration of Competing Interests

JLB is on the board of wFluidx, Inc., owns stock in Orchard Therapeutics, and has consulted for Bluebird bio, Calico Life Sciences, Denali Therapeutics, Enzyvant, and Neurogene. Otherwise, the authors have no conflicts of interest to declare.

788

789 **References**

790 Abbink TEM, Wisse LE, Jaku E, Thiecke MJ, Voltolini-González D, Fritsen H, Bobeldijk S, Ter
791 Braak TJ, Polder E, Postma NL, Bugiani M, Struijs EA, Verheijen M, Straat N, van der Sluis S,
792 Thomas AAM, Molenaar D, van der Knaap MS. Vanishing white matter: deregulated integrated
793 stress response as therapy target. Ann Clin Transl Neurol. 2019 Aug;6(8):1407-1422.

794

795 Atzmon A, Herrero M, Sharet-Eshed R, Gilad Y, Senderowitz H, Elroy-Stein O. Drug Screening
796 Identifies Sigma-1-Receptor as a Target for the Therapy of VWM Leukodystrophy. Front Mol
797 Neurosci. 2018;11:336.

798

799 Bond S, Lopez-Lloreda C, Gannon PJ, Akay-Espinoza C, Jordan-Sciutto KL. The Integrated
800 Stress Response and Phosphorylated Eukaryotic Initiation Factor 2α in Neurodegeneration. J
801 Neuropathol Exp Neurol. 2020 Feb 1;79(2):123-143.

802

803 Bonkowsky, J.L., Wang, X., Fujimoto, E., Lee, J.E., Chien, C.B. and Dorsky, R.I. (2008)
804 Domain-specific regulation of foxP2 CNS expression by lef1. BMC developmental biology, 8,
805 103.

806

807 Brady LK, Wang H, Radens CM, Bi Y, Radovich M, Maity A, Ivan C, Ivan M, Barash Y,
808 Koumenis C. Transcriptome analysis of hypoxic cancer cells uncovers intron retention in
809 EIF2B5 as a mechanism to inhibit translation. PLoS Biol. 2017 Sep 29;15(9):e2002623.

810

811 Bugiani M, Boor I, Powers JM, Scheper GC, van der Knaap MS. Leukoencephalopathy with
812 vanishing white matter: a review. J Neuropathol Exp Neurol. 2010;69:987-96.
813
814 Carra-Dalliere C, Horzinski L, Ayrignac X, et al. Natural history of adult-onset eIF2B-related
815 disorders: a multicentric survey of 24 cases [in French]. Rev Neurol (Paris). 2011;167:802–811.
816
817 Dooves S, Bugiani M, Postma NL, Polder E, Land N, Horan ST, van Deijk AL, van de Kreeke
818 A, Jacobs G, Vuong C, Klooster J, Kamermans M, Wortel J, Loos M, Wisse LE, Scheper GC,
819 Abbink TE, Heine VM, van der Knaap MS. Astrocytes are central in the pathomechanisms of
820 vanishing white matter. J Clin Invest. 2016;126:1512-24.
821
822 Fogli A, Schiffmann R, Bertini E, Ughetto S, Combes P, Eymard-Pierre E, Kaneski CR, Pineda
823 M, Troncoso M, Uziel G, Surtees R, Pugin D, Chaunu MP, Rodriguez D, Boespflug-Tanguy O.
824 The effect of genotype on the natural history of eIF2B-related leukodystrophies. Neurology.
825 2004;62:1509–1517.
826
827 Geva M, Cabilly Y, Assaf Y, Mindroul N, Marom L, Raini G, Pinchasi D, Elroy-Stein O. A
828 mouse model for eukaryotic translation initiation factor 2B-leucodystrophy reveals abnormal
829 development of brain white matter. Brain. 2010;133(Pt 8):2448-61.
830
831 Hamilton EMC, van der Lei HDW, Vermeulen G, Gerver JAM, Lourenço CM, Naidu S,
832 Mierzewska H, Gemke RJBJ, de Vet HCW, Uitdehaag BMJ, Lissenberg-Witte BI; VWM
833 Research Group, van der Knaap MS. Natural History of Vanishing White Matter. Ann

834 Neurol. 2018;84:274-288.

835

836 Harding HP, Novoa I, Zhang Y, Zeng H, Wek R, Schapira M, Ron D. Regulated translation
837 initiation controls stress-induced gene expression in mammalian cells. Mol Cell. 2000
838 Nov;6(5):1099-108.

839

840 Jennings MD, Pavitt GD. A new function and complexity for protein translation initiation factor
841 eIF2B. Cell Cycle. 2014;13(17):2660-5.

842

843 Krishnamoorthy T, Pavitt GD, Zhang F, Dever TE, Hinnebusch AG. 2001. Tight binding of the
844 phosphorylated alpha subunit of initiation factor 2 (eIF2alpha) to the regulatory subunits of
845 guanine nucleotide exchange factor eIF2B is required for inhibition of translation initiation.
846 Molecular and Cellular Biology 21:5018–5030.

847

848 Kucenas, S., Takada, N., Park, H.C., Woodruff, E., Broadie, K. and Appel, B. (2008) CNS-
849 derived glia ensheath peripheral nerves and mediate motor root development. Nature
850 neuroscience, 11, 143-151.

851

852 Labauge P, Horzinski L, Ayrignac X, Blanc P, Vukusic S, Rodriguez D, Mauguiere F, Peter L,
853 Goizet C, Bouhour F, Denier C, Confavreux C, Obadia M, Blanc F, de Sèze J, Fogli A,
854 Boespflug-Tanguy O. Natural history of adult-onset eIF2B-related disorders: a multi-centric
855 survey of 16 cases. Brain. 2009;132(Pt 8):2161-9.

856

857 Lambert, A.M., Bonkowsky, J.L., Masino, M.A. (2012) The conserved dopaminergic
858 diencephalospinal tract mediates vertebrate locomotor development in zebrafish
859 larvae, Journal of Neuroscience, 32,13488-500.
860
861 Lambert CJ, Freshner BC, Chung A, Stevenson TJ, Bowles DM, Samuel R, Gale BK,
862 Bonkowsky JL. An automated system for rapid cellular extraction from live zebrafish embryos
863 and larvae: Development and application to genotyping. PLoS One. 2018 Mar
864 15;13(3):e0193180.
865
866 Leegwater PA, Vermeulen G, Ko¨ nst AA, Naidu S, Mulders J, Visser A, Kersbergen P, Mobach
867 D, Fonds D, van Berkel CG, Lemmers RJ, Frants RR, Oudejans CB, Schutgens RB, Pronk JC,
868 van der Knaap MS. 2001. Subunits of the translation initiation factor eIF2B are mutant in
869 leukoencephalopathy with vanishing white matter. Nature Genetics 29:383–388.
870
871 Lin Y, Pang X, Huang G, Jamison S, Fang J, Harding HP, Ron D, Lin W. Impaired eukaryotic
872 translation initiation factor 2B activity specifically in oligodendrocytes reproduces the pathology
873 of vanishing white matter disease in mice. J Neurosci. 2014;34:12182-91.
874
875 Liu R, van der Lei HD, Wang X, Wortham NC, Tang H, van Berkel CG, Mufunde TA, Huang
876 W, van der Knaap MS, Scheper GC, Proud CG. Severity of vanishing white matter disease does
877 not correlate with deficits in eIF2B activity or the integrity of eIF2B complexes. Hum Mutat.
878 2011 Sep;32(9):1036-45.
879

880 Moon SL, Parker R. Analysis of eIF2B bodies and their relationships with stress granules and P-
881 bodies. Sci Rep. 2018 Aug 16;8(1):12264.
882
883 Pakos-Zebrucka K, Koryga I, Mnich K, Ljujic M, Samali A, Gorman AM. The integrated stress
884 response. EMBO Rep. 2016 Oct;17(10):1374-1395.
885
886 Park, H.C., Boyce, J., Shin, J. and Appel, B. (2005) Oligodendrocyte specification in zebrafish
887 requires notch-regulated cyclin-dependent kinase inhibitor function. The Journal of
888 neuroscience, 25, 6836-6844.
889
890 Pronk JC, van Kollenburg B, Scheper GC, van der Knaap MS. Vanishing white matter disease: a
891 review with focus on its genetics. Ment Retard Dev Disabil Res Rev. 2006;12(2):123-8.
892
893 Sekine Y, Zyryanova A, Crespillo-Casado A, Amin-Wetzel N, Harding HP, Ron D. Paradoxical
894 Sensitivity to an Integrated Stress Response Blocking Mutation in Vanishing White Matter Cells.
895 PLoS One. 2016 Nov 3;11(11):e0166278.
896
897 Sidrauski C, Acosta-Alvear D, Khoutorsky A, Vedantham P, Hearn BR, Li H, Gamache K,
898 Gallagher CM, Ang KK- H, Wilson C, Okreglak V, Ashkenazi A, Hann B, Nader K, Arkin MR,
899 Renslo AR, Sonenberg N, Walter P. 2013. Pharmacological brake-release of mRNA translation
900 enhances cognitive memory. eLife 2:e00498.
901

902 Sidrauski C, Tsai JC, Kampmann M, Hearn BR, Vedantham P, Jaishankar P, Sokabe M, Mendez
903 AS, Newton BW, Tang EL, Verschueren E, Johnson JR, Krogan NJ, Fraser CS, Weissman JS,
904 Renslo AR, Walter P. Pharmacological dimerization and activation of the exchange factor
905 eIF2B antagonizes the integrated stress response. Elife. 2015;4:e07314.
906
907 Sievers, F., Wilm, A., Dineen, D., Gibson, T.J., Karplus, K., Li, W., Lopez, R., McWilliam, H.,
908 Remmert, M., Soding, J. et al. (2011) Fast, scalable generation of high-quality protein multiple
909 sequence alignments using Clustal Omega. Molecular systems biology, 7, 539.
910
911 Simossis, V.A. and Heringa, J. (2005) PRALINE: a multiple sequence alignment toolbox that
912 integrates homology-extended and secondary structure information. Nucleic acids research, 33,
913 W289-294.
914
915 Song H, Haeri S, Vogel H, van der Knaap M, Van Haren K. Postmortem Whole Exome
916 Sequencing Identifies Novel EIF2B3 Mutation With Prenatal Phenotype in 2 Siblings. J Child
917 Neurol. 2017 Sep;32(10):867-870.
918
919 Thisse C, Thisse B. High-resolution in situ hybridization to whole-mount zebrafish embryos. Nat
920 Protoc. 2008;3(1):59-69.
921
922 Tsai JC, Miller-Vedam LE, Anand AA, Jaishankar P, Nguyen HC, Renslo AR, Frost A, Walter
923 P. 2018. Structure of the nucleotide exchange factor eIF2B reveals mechanism of memory-
924 enhancing molecule. Science 359:eaaq0939.

van der Knaap MS, Barth PG, Gabreëls FJ, Franzoni E, Begeer JH, Stroink H, Rotteveel JJ, Valk J. A new leukoencephalopathy with vanishing white matter. Neurology. 1997 Apr;48(4):845-55.

van der Knaap MS, Kamphorst W, Barth PG, Kraaijeveld CL, Gut E, Valk J. Phenotypic variation in leukoencephalopathy with vanishing white matter. Neurology. 1998 Aug;51(2):540-7.

van der Knaap MS, van Berkel CG, Herms J, van Coster R, Baethmann M, Naidu S, Boltshauser E, Willemsen MA, Plecko B, Hoffmann GF, Proud CG, Scheper GC, Pronk JC. eIF2B-related disorders: antenatal onset and involvement of multiple organs. Am J Hum Genet. 2003 Nov;73(5):1199-207.

van der Knaap MS, Pronk JC, Scheper GC. Vanishing white matter disease. Lancet Neurol. 2006;5:413-23.

van der Voorn JP, van Kollenburg B, Bertrand G, Van Haren K, Scheper GC, Powers JM, van der Knaap MS. 2005. The unfolded protein response in vanishing white matter disease. Journal of Neuropathology & Experimental Neurology 64:770–775.

Van Haren K, van der Voorn JP, Peterson DR, van der Knaap MS, Powers JM. The life and death of oligodendrocytes in vanishing white matter disease. J Neuropathol Exp Neurol. 2004 Jun;63(6):618-30.

van Kollenburg B, van Dijk J, Garbern J, Thomas AA, Scheper GC, Powers JM, van der Knaap MS. 2006. Glia- specific activation of all pathways of the unfolded protein response in vanishing white matter disease. Journal of Neuropathology and Experimental Neurology 65:707–715.

Watatani Y, Ichikawa K, Nakanishi N, Fujimoto M, Takeda H, Kimura N, Hirose H, Takahashi S, Takahashi Y. Stress-induced translation of ATF5 mRNA is regulated by the 5'-untranslated region. J Biol Chem. 2008 Feb 1;283(5):2543-53.

Wisse LE, Penning R, Zaal EA, van Berkel CGM, Ter Braak TJ, Polder E, Kenney JW, Proud CG, Berkers CR, Altelaar MAF, Speijer D, van der Knaap MS, Abbink TEM. Proteomic and Metabolomic Analyses of Vanishing White Matter Mouse Astrocytes Reveal Deregulation of ER Functions. Front Cell Neurosci. 2017 Dec 20;11:411.

Wong YL, LeBon L, Edalji R, Lim HB, Sun C, Sidrauski C. The small molecule ISRIB rescues the stability and activity of Vanishing White Matter Disease eIF2B mutant complexes. Elife. 2018 Feb 28;7.

Wong YL, LeBon L, Basso AM, Kohlhaas KL, Nikkel AL, Robb HM, Donnelly-Roberts DL, Prakash J, Swensen AM, Rubinstein ND, Krishnan S, McAllister FE, Haste NV, O'Brien JJ, Roy M, Ireland A, Frost JM, Shi L, Riedmaier S, Martin K, Dart MJ, Sidrauski C. eIF2B activator prevents neurological defects caused by a chronic integrated stress response. Elife. 2019;8. pii: e42940.

971

972 Xing, L., Quist, T.S., Stevenson, T.J., Dahlem, T.J. and Bonkowsky, J.L. (2014) Rapid and
973 efficient zebrafish genotyping using PCR with high-resolution melt analysis. Journal of
974 visualized experiments : JoVE, e51138.

975

976

977

978 **Supplemental Figure 1.** MRI images of adult wild-type control siblings and *eif2b5*$^{zc103/zc103}$ fish,
979 showing decreased head and body size. A) Demonstration of orientation used for length, width,
980 and height measurements of head. B) MRI images, and quantification, of control compared to
981 mutant, demonstrating decreased sizes.
982

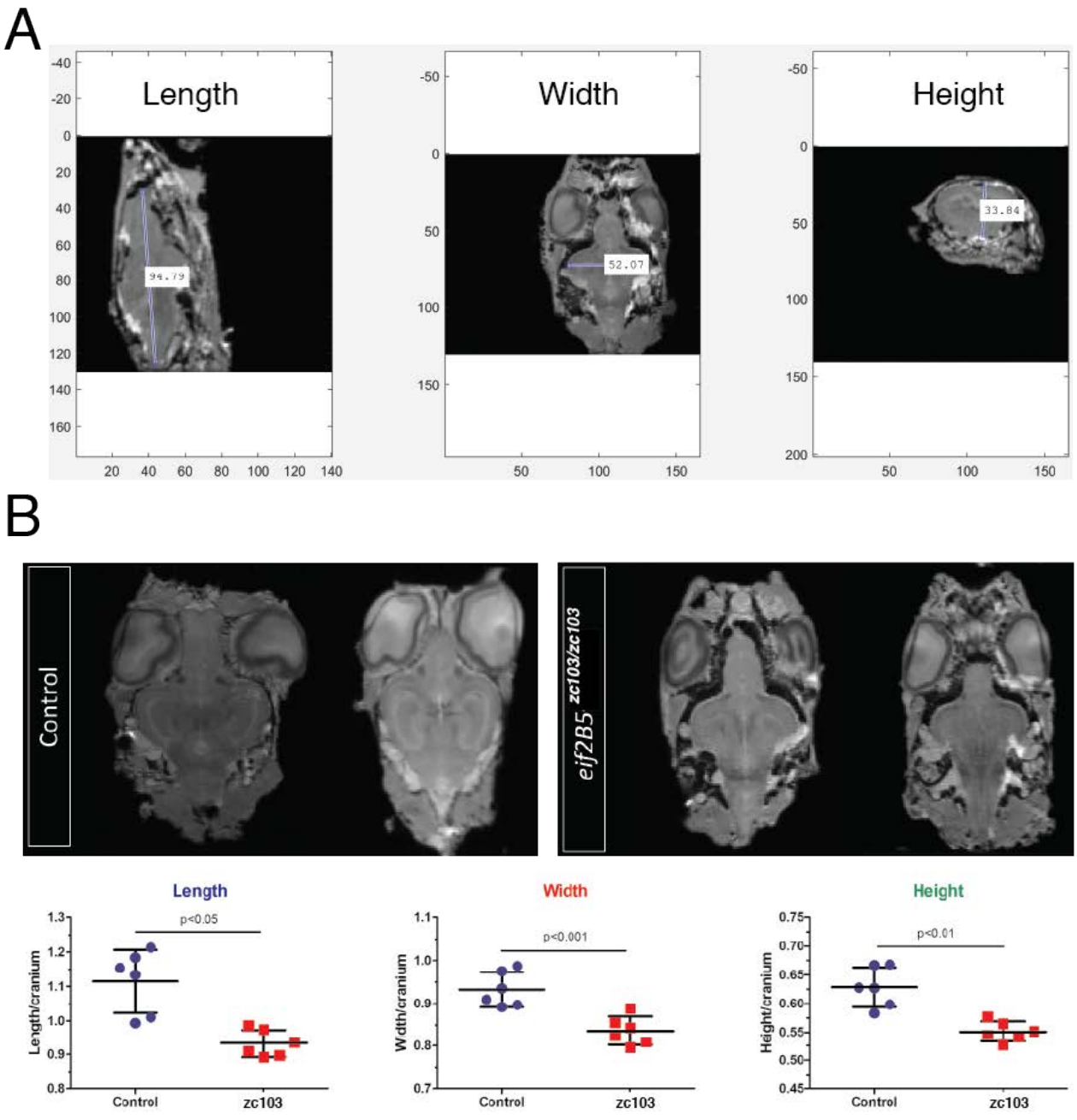

983